



Evidence for Centrifugal Breakout around the Young M Dwarf TIC 234284556

Elsa K. Palumbo¹ , Benjamin T. Montet^{2,3} , Adina D. Feinstein^{4,7} , Luke G. Bouma⁵ , Joel D. Hartman⁵ ,
Lynne A. Hillenbrand¹, Michael A. Gully-Santiago⁶ , and Kirsten A. Banks²

¹ Department of Astronomy, MC 249-17, California Institute of Technology, Pasadena, CA 91125, USA; epalumbo@caltech.edu

² School of Physics, University of New South Wales, Sydney, NSW 2052, Australia

³ UNSW Data Science Hub, University of New South Wales, Sydney, NSW 2052, Australia

⁴ Department of Astronomy and Astrophysics, University of Chicago, 5640 S. Ellis Ave., Chicago, IL 60637, USA

⁵ Department of Astrophysical Sciences, Princeton University, 4 Ivy Lane, Princeton University, Princeton, NJ 08544, USA

⁶ Department of Astronomy, University of Texas at Austin, 2515 Speedway, Stop C1400, Austin, TX 78712-1205, USA

Received 2021 July 2; revised 2021 November 9; accepted 2021 November 9; published 2022 January 26

Abstract

Magnetospheric clouds have been proposed as explanations for depth-varying dips in the phased light curves of young, magnetically active stars such as σ Ori E and RIK-210. However, the stellar theory that first predicted magnetospheric clouds also anticipated an associated mass-balancing mechanism known as centrifugal breakout for which there has been limited empirical evidence. In this paper, we present data from the Transiting Exoplanet Survey Satellite, Las Cumbres Observatory, All-Sky Automated Survey for Supernovae, and Veloce on the 45 Myr M3.5 star TIC 234284556, and propose that it is a candidate for the direct detection of centrifugal breakout. In assessing this hypothesis, we examine the sudden (~ 1 day timescale) disappearance of a previously stable (~ 1 month timescale) transit-like event. We also interpret the presence of an anomalous brightening event that precedes the disappearance of the signal, analyze rotational amplitudes and optical flaring as a proxy for magnetic activity, and estimate the mass of gas and dust present immediately prior to the potential breakout event. After demonstrating that our spectral and photometric data support a magnetospheric cloud and centrifugal breakout model and disfavor alternate scenarios, we discuss the possibility of a coronal mass ejection or stellar wind origin of the corotating material and we introduce a reionization mechanism as a potential explanation for more gradual variations in eclipse parameters. Finally, after comparing TIC 234284556 with previously identified “flux-dip” stars, we argue that TIC 234284556 may be an archetypal representative of a whole class of young, magnetically active stars.

Unified Astronomy Thesaurus concepts: M dwarf stars (982); Stellar coronal mass ejections (1881); Stellar magnetic fields (1610); Stellar flares (1603); Stellar winds (1636)

1. Introduction

Young ($\lesssim 100$ Myr) stars have important implications for planet formation, evolution, and habitability because they tend to be magnetically active (e.g., Feigelson et al. 1991, p. 658; Vidotto et al. 2014b) with strong (kG) magnetic fields, their planets tend to be rapidly evolving (Mann et al. 2020) and their protoplanetary disks may not yet have dissipated (e.g., Williams & Cieza 2011). In particular, they can teach us about how, when, and why atmospheric evolution, planetary migration, and other dynamical interactions take place (e.g., Rizzuto et al. 2020). For example, some pre-main-sequence stars have X-ray flares that, at their peak luminosity, release more energy in one second than the total X-ray energy from any known solar flare (Getman & Feigelson 2021). The ionizing radiation from such flares impacts accretion, disk chemistry, and atmospheric erosion (Benz & Güdel 2010; Waggoner & Cleeves 2019). Similarly, coronal mass ejections (CMEs)—mass-loss events potentially connected to such flaring activity—may influence radionuclide production in protoplanetary disks, planetary

dynamos, and the clearing of debris disks (Osten & Wolk 2015).

Young stars exhibit many different classes of photometric variability. One type is the quasi-periodic dimming events of “dipper” stars, likely caused by nonuniformly distributed gas and dust in the protoplanetary disk (Bodman et al. 2017; Cody & Hillenbrand 2010; Ansdell et al. 2016). Dippers are very common, accounting for 20%–30% of young stellar objects (McGinnis et al. 2015; Ansdell et al. 2020). Their deep (up to 50%), often aperiodic eclipse events (Stauffer et al. 2015; Cody & Hillenbrand 2018) and strong infrared excesses (Hedges et al. 2018) make them easily detectable in time-series photometry and therefore useful for studying disk evolution and planet formation.

More recently, stars without significant infrared excesses but with rapid, periodic photometric variability have been identified. Stauffer et al. (2017, 2018, 2021) and Zhan et al. (2019) describe three families of young M dwarfs that exhibit periodic photometric variability that appears to be synchronous with stellar rotation but that does not fit cleanly into previously established categories:

1. Scallop shell stars—rapidly rotating ($P_{\text{rot}} < 0.65$ days) M dwarfs whose light curves exhibit multiple wavelike dips that are typically stable over ~ 75 – 80 day timescales. Such dips have been seen to undergo sudden morphological changes (Stauffer et al. 2017).

⁷ NSF Graduate Research Fellow.



2. Persistent flux-dip stars—stars with discrete triangularly shaped dips in their light curves. Similarly to scallop shells, dimming events have been seen to suddenly change in depth (Stauffer et al. 2017).
3. Transient flux-dip stars—stars with a single prominent and roughly triangular dip. The depth of the dip may vary significantly from cycle to cycle, with more gradual changes sometimes occurring over longer timescales (Stauffer et al. 2017). RIK-210 is one particularly well-characterized example of such an object (David et al. 2017).

Work by Günther et al. (2020a) has since shown that the distinction between scallop shells and flux-dip stars may be due only to an observational bias and their quick rotation periods. These authors suggest that a low-cadence sampling rate leads to smearing which makes flux-dip stars look like scallop shells.

One well-known example of a flux-dip star is the 7–10 Myr old PTFO 8-8695, which exhibits 0.45 day period transit-like dips with shapes, depths, and durations that have varied over a decade of observation and that are synchronous with the host star’s rotation (van Eyken et al. 2012; Yu et al. 2015). The proposed explanations for the dips for this system have ranged from a precessing Jovian planet (Barnes et al. 2013) to an accretion hotspot (Yu et al. 2015) or even a small dusty planet (Tanimoto et al. 2020). More recently, Bouma et al. (2020a) have suggested circumstellar material as a likely explanation based on a synthesis of earlier ground-based observations with data from the Transiting Exoplanet Survey Satellite (TESS; Ricker et al. 2014).

The flux-dip stars also have a number of massive analogs (e.g. Bohlender & Monin 2011; Grunhut et al. 2013; Rivinius et al. 2013; Shultz et al. 2020). Of these, the archetypal example is σ Ori E, a ≈ 1.1 Myr, B2 star in the Orion complex (Townsend et al. 2013). σ Ori E’s light curve features distinctive double dips with periodicity matching that of the star’s rotational period (e.g., Townsend et al. 2013). Although these dips are morphologically similar to the eclipses of an eclipsing binary (Townsend 2007), radial-velocity data has excluded a massive ($>0.04M_{\odot}/\sin i$) companion (Groote & Hunger 1977).

Theories of the origin of σ Ori E’s dips center around magnetic interactions. In particular, Landstreet & Borra (1978) discovered that magnetically trapped plasma could recreate σ Ori E’s photometric and spectroscopic variability, with Townsend & Owocki (2005) formalizing the underlying theory via a Rigidly Rotating Magnetosphere (RRM) model.

Under this model, σ Ori E’s dips are caused by two corotating circumstellar plasma clouds originating from stellar winds (Townsend & Owocki 2005). Because of σ Ori E’s strong magnetic field (7.3–7.8 kG at the poles; Oksala et al. 2015) and rapid rotation, the stellar wind would accumulate into relatively dense, stable regions within the star’s magnetic field (Owocki & Cranmer 2018). While the RRM model successfully provided a theoretical basis for σ Ori E’s photometric and spectroscopic signatures, Oksala et al. (2015) have since highlighted the need to incorporate additional physics into the RRM model. Regardless of model, magnetospheric clouds are widely accepted for the origin of σ Ori E’s variability (Townsend & Owocki 2005; Oksala et al. 2012; Townsend et al. 2013) and they have also been used to explain the dips of the flux-dip stars (David et al. 2017; Stauffer et al. 2017).

Over time, material continues to accumulate in the magnetospheric clouds, but since there is a critical point beyond which the magnetic force can no longer contain the magnetospheric cloud’s material by balancing the centrifugal force, a mass-balancing mechanism is required (Owocki & Cranmer 2018; Shultz et al. 2020). One such proposed mass-balancing mechanism is centrifugal breakout, in which the ionized gas and dust that make up the magnetospheric clouds accumulate, dragging the magnetic field lines along with them until the cloud becomes so massive that the magnetic loops constraining the corotating material are stressed and ultimately broken. This centrifugal breakout event would coincide with the previously trapped material being suddenly expelled, with the magnetic field lines reconnecting immediately afterward (e.g., Townsend & Owocki 2005).

This mechanism has a number of advantages: (1) it can be derived from first principles (see Townsend & Owocki 2005), (2) it is consistent with magnetohydrodynamic simulations (ud-Doula et al. 2006; Ud-Doula et al. 2008), and (3) it is supported by stars’ observed $H\alpha$ emission (Owocki et al. 2020; Shultz et al. 2020). However, Townsend et al. (2013) did not detect any photometric evidence of a breakout event around σ Ori E—nor did the more recent work of Shultz et al. (2020) in spectroscopic data spanning 20 yr around one of σ Ori E’s B-type analogs—leading to a consideration of alternate mechanisms, such as the diffusion-plus-drift model of Owocki & Cranmer (2018). Debate over centrifugal breakout’s importance continues today, even though Owocki et al. (2020) have addressed some of the original objections to centrifugal breakout brought up by Townsend et al. (2013).

Here, we consider the light curve of TIC⁸ 234284556⁹, a ≈ 45 million year old, $0.42 \pm 0.02M_{\odot}$ star in the Tucana–Horologium association (Kraus et al. 2014) which has corotating dip-like features that resemble those of PTFO 8-8695, σ Ori E, and the young low-mass stars observed by Stauffer et al. (2018) and Zhan et al. (2019). Notably, we observe a 1.2% deep dip that had been present in data from the previous 24 days disappear within a ~ 1 day interval. We interpret this as evidence for a potential centrifugal breakout event, with more gradual changes in eclipse parameters hinting at a separate role for an additional mass-balancing mechanism. This signal matches observationally with other eclipses that have been attributed to magnetospheric clouds, as well as to the numerical simulations of magnetospheric clouds produced by Townsend (2008).

TIC 234284556 stands out because it is relatively bright, with $I = 11.68$ (Denis Consortium 2005), and nearby, at 44.102 ± 0.028 pc (Bailer-Jones et al. 2021), compared to ≈ 130 pc for the younger transient flux-dip stars in the Taurus, Upper Sco, and UCL/LCC clusters. This star has been observed by the TESS mission for \sim three sectors over two years. Besides being a promising target for follow-up observations, TIC 234284556’s low mass ($0.422 M_{\odot}$) also hints at alternatives to σ Ori E’s stellar wind mechanism for mass accumulation, such as CMEs.

This paper is organized as follows: in Section 2, we present our photometric and spectroscopic observations of

⁸ TESS Input Catalog (TIC; Stassun et al. 2018).

⁹ This star is also known as UCAC4 135-177645, 2MASS J22223966-6303258, WISE J222239.75-630326.5, DENIS J222239.6-630325, UPM J2222-6303, Gaia EDR3 6405089921141776128, and APASS 31766662.

Table 1
Wavelength-specific Magnitudes for TIC 234284556

Bandpass	Value	Reference
WISE4 [22.24 μm]	8.644 ± 0.345	Cutri et al. (2021)
WISE3 [11.56 μm]	8.867 ± 0.027	Cutri et al. (2021)
WISE2 [4.600 μm]	9.012 ± 0.020	Cutri et al. (2021)
WISE1 [3.350 μm]	9.192 ± 0.024	Cutri et al. (2021)
<i>H</i> [2.159 μm]	9.345 ± 0.023	Cutri et al. (2003)
<i>K</i> [1.662 μm]	9.588 ± 0.026	Cutri et al. (2003)
<i>j</i> [1.235 μm]	10.183 ± 0.024	Cutri et al. (2003)
RP [0.799 μm]	11.9489 ± 0.0055	Gaia Collaboration (2020)
<i>i</i> [0.759 μm]	12.489 ± 0.04	Zacharias et al. (2012)
<i>G</i> [0.673 μm]	13.1820 ± 0.0030	Gaia Collaboration (2020)
<i>r</i> [0.617 μm]	14.038 ± 0.00	Zacharias et al. (2012)
<i>V</i> [0.544 μm]	14.645 ± 0.02	Zacharias et al. (2012)
BP [0.532 μm]	14.8089 ± 0.0076	Gaia Collaboration (2020)
<i>g</i> [0.469 μm]	15.338 ± 0.01	Zacharias et al. (2012)
<i>B</i> [0.436 μm]	16.245 ± 0.08	Zacharias et al. (2012)

TIC 234284556, which include data from TESS, the All-Sky Automated Survey for Supernovae (ASAS-SN), the Veloce–Rosso spectrograph, and the Las Cumbres Observatory (LCO). In Section 3, we present our analysis of these data and examine depth variations, flare rates, and other relevant features of the light curves. In Sections 4 and 5, we discuss potential origins of the observed dips and compare our findings with the theoretical predictions of centrifugal breakout. In Section 6, we introduce a mechanism that could be behind more gradual changes in dip size, discuss stellar wind and CME sources of the corotating material, and examine our system in the broader context of young stars with similar variability. Finally, Section 7 summarizes our findings, their implications, and the role of future work.

2. Observations

2.1. Stellar Parameters

TIC 234284556 is an M3.5 star and a bona fide member of the Tucana–Horologium association (Tuc–Hor), a young moving group with an age of 35–45 Myr (Bell et al. 2015; Crundall et al. 2019). Its membership has been previously confirmed based on its proper motion and spectroscopic signatures of youth (Kraus et al. 2014). Moreover, its short and high-amplitude rotational signal is qualitatively consistent with what would be expected from a young star (e.g., Reinhold & Gizon 2015). Young, low-mass stars like TIC 234284556 tend to have strong magnetic fields, typically ranging from 0.1 to 10 kG (Gregory et al. 2012; Shulyak et al. 2019), and TIC 234284556’s stellar parameters, regular flaring, and rotational signal suggest that it likely is similar.

Using data from 2MASS, WISE, SDSS, APASS, Gaia EDR3, and Gaia (Table 1), we constructed the spectral energy distribution (SED) of our target (Figure 1), comparing to the NextGen model atmosphere library for stars of similar temperature and metallicity (Hauschildt et al. 1999). We find the SED is well-described by a 3100 \pm 60 K model atmosphere with no infrared excess or interstellar extinction; this temperature is consistent with the estimate of 3249 \pm 157 K provided by Stassun et al. (2019). The lack of IR excess indicates that the primordial protoplanetary disk has already dissipated, effectively ruling out a dip-causing mechanism due to a massive, extended disk, as observed in dipper stars.

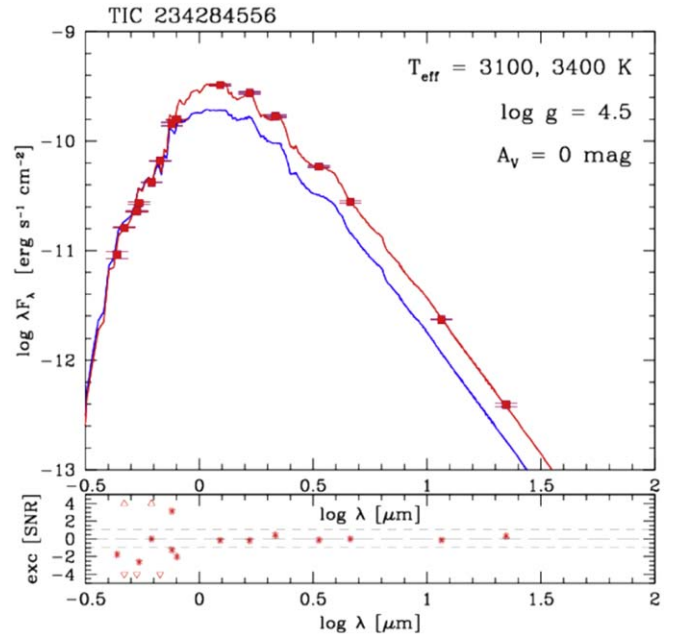


Figure 1. SED for TIC 234284556 along with atmospheric models at the approximate $\pm 1\sigma$ range of the Stassun et al. (2019) temperature estimate for this star, with the cooler 3100 K model in red and the hotter 3400 K model in blue. For low levels of extinction (A_v), this plot suggests an effective temperature near the lower limit presented in Stassun et al. (2019). Unlike the dipper stars, but like the stars described by Stauffer et al. (2017), Stauffer et al. (2018), Zhan et al. (2019), and Stauffer et al. (2021), TIC 234284556 lacks any detectable infrared excess, indicating that its dimming events are not caused by an extended protoplanetary disk.

The SED also allows us to place a numerical upper limit on the amount of dust present at the Kepler corotation radius r_K , the orbital distance where an object’s orbital period coincides with the stellar rotational period, which is given by

$$r_K = \left(\frac{GM_* P_{\text{rot}}^2}{4\pi^2} \right)^{1/3}, \quad (1)$$

where P_{rot} is the rotational period of the star, M_* its mass, and G is the gravitational constant.

To estimate the amount of dust that could exist near the corotation radius given the observed SED, we first found the T_{eff} of material at the Kepler corotation radius to be $T_K = 806 \pm 41$ K. This temperature corresponds to emission at wavelengths near the WISE1 bandpass near 3.6 μm . We therefore used the uncertainty from the WISE1 observation to calculate the increase in flux density at 3.6 μm that we can attribute to dust. Finally, using stellar parameters from Table 2 and Equation (1) from Buemi et al. (2007), we find our 1σ estimate for the dust mass to be

$$M_{\text{dust}} = 1.3 \times 10^{-4} M_{\odot} \left(\frac{\chi_{\nu}}{1 \text{ cm}^2 \text{ g}^{-1}} \right)^{-1}, \quad (2)$$

where χ_{ν} is the opacity of the dust at the observing frequency. For typical opacities ($\chi_{\nu} = 1\text{--}10 \text{ cm}^2 \text{ g}^{-1}$) this would correspond to a dust mass of 4.2 to 42 M_{\oplus} .

TIC 234284556 has a renormalized unit weight error (RUWE) of 1.348 (Gaia Collaboration 2020), which might be considered suggestive of astrometric binarity (e.g., Belokurov et al. 2020). However, Figure 2’s plot of the RUWE of the high-confidence Tuc–Hor members from Gagné et al. (2018)

Table 2
Summary of Stellar Parameters for TIC 234284556

Parameter	Value	Reference
TESS designation	TIC 234284556	Stassun et al. (2019)
Gaia EDR3 designation	6405089921141776128	
R.A. [J2000]	22h 22m 39.69s	Gaia Collaboration (2020)
Decl. [J2000]	$-63^{\circ} 03' 25.83''$	Gaia Collaboration (2020)
Spectral type	M3.5	Kraus et al. (2014)
m_{TESS}	11.8868 ± 0.0080	Stassun et al. (2019)
I_{mag}	11.68 ± 0.03	Denis Consortium (2005)
$V \sin i$ [km s^{-1}]	11.9 ± 0.4	This work
P_{rot} [days]	1.1066 ± 0.0003	This work
Distance [pc]	44.102 ± 0.028	Bailer-Jones et al. (2021)
Mass [M_{\odot}]	0.422 ± 0.020	Stassun et al. (2019)
Radius [R_{\odot}]	0.428 ± 0.013	Stassun et al. (2019)
T_{eff} [K]	3100 ± 60	This work
Age [Myr]	45 ± 4	Bell et al. (2015)
$\text{Log}_{10}(g_{*})$ [cm s^{-2}]	4.8014 ± 0.0051	Stassun et al. (2019)
r_K [R_{*}]	7.89 ± 0.27	This work
i_{rot} [$^{\circ}$]	37.5 ± 2.0	This work

shows a color dependence, with Tuc–Hor members of a similar color having similar RUWE values, casting doubt on the binary interpretation. For an independent confirmation of this assessment, we plotted the Hertzsprung–Russel diagram for the same list of high-confidence Tuc–Hor members (Figure 2), finding TIC 234284556 to be consistent with the expected position for a single star.

2.2. Transiting Exoplanet Survey Satellite

TESS (Ricker et al. 2014) observed TIC 234284556 in three sectors over two years: Sector 1 (2018 July 25–2018 August 22), Sector 27 (2020 July 4–2020 July 30), and Sector 28 (2020 July 30–2020 August 26). TIC 234284556 was preselected as a short-cadence target through the TESS Guest Investigator program and is also available in the full-frame images (FFIs).¹⁰

As a precaution against data-processing effects, we compared results from both short-cadence and FFI light curves throughout this work, where we relied on the open-source Python package *eleanor* (Feinstein et al. 2019) to extract light curves from the FFIs. However, for our final analysis, we used all of the two-minute-cadence TESS data produced by the NASA Ames’ Science Processing and Operations Center (SPOC) pipeline (Jenkins et al. 2016), only neglecting cadences flagged by that pipeline as having potential quality concerns. The resulting short-cadence TESS light curves are shown in Figure 3, with phase-folded and stacked versions of the same data in Figure 4.

In our original data processing, we applied Gaussian process (GP) regression to the long-cadence data in order to model TIC 234284556’s rotational signal. We used the `gp.terms.RotationTerm` kernel from the Python package *exoplanet* (Foreman-Mackey et al. 2017, 2020) to model stellar

¹⁰ The target was proposed in program GI G011175, G011266, G011180, G03265, and G03226.

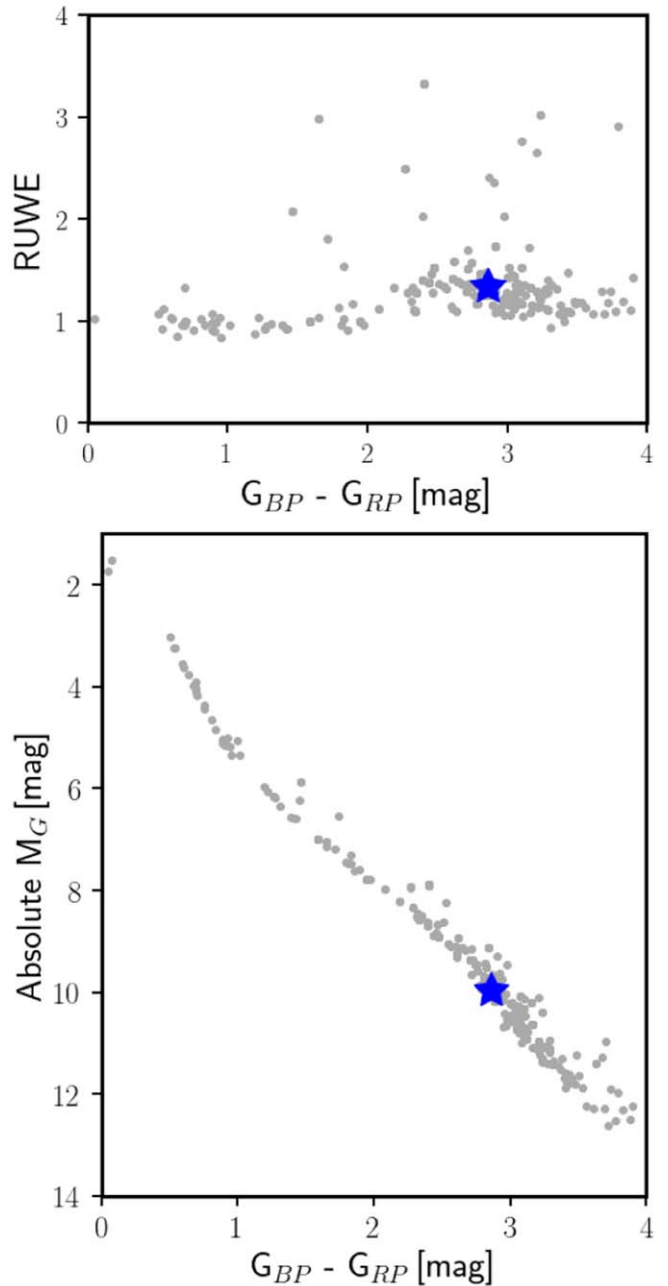


Figure 2. Evidence for nonbinarity of TIC 234284556. Point estimates for TIC 234284556 (blue star) and all other high-confidence Tuc–Hor members (gray circles) are shown, where a difference of Gaia’s Rp and Bp bandpasses is used to quantify a star’s color, a proxy for spectral type. Top panel: assessing astrometric binarity. Note the color dependence of typical RUWE values, which casts doubt on the interpretation that TIC 234284556’s RUWE of 1.348 is indicative of it being an astrometric binary. Bottom panel: assessing photometric binarity. Note that the point estimate for TIC 234284556 is not above the intrinsic scatter, suggesting that our target is not a photometric binary.

variability as the combined behavior of two underdamped simple harmonic oscillators, one with a period corresponding to the rotational period of the star, and the other with half that period. We then used an iterative approach to define hyperparameters describing the GP, and to identify and mask outliers.

With this GP fit, we removed a model of stellar rotation from the TESS short-cadence data. Inspecting the light curve with

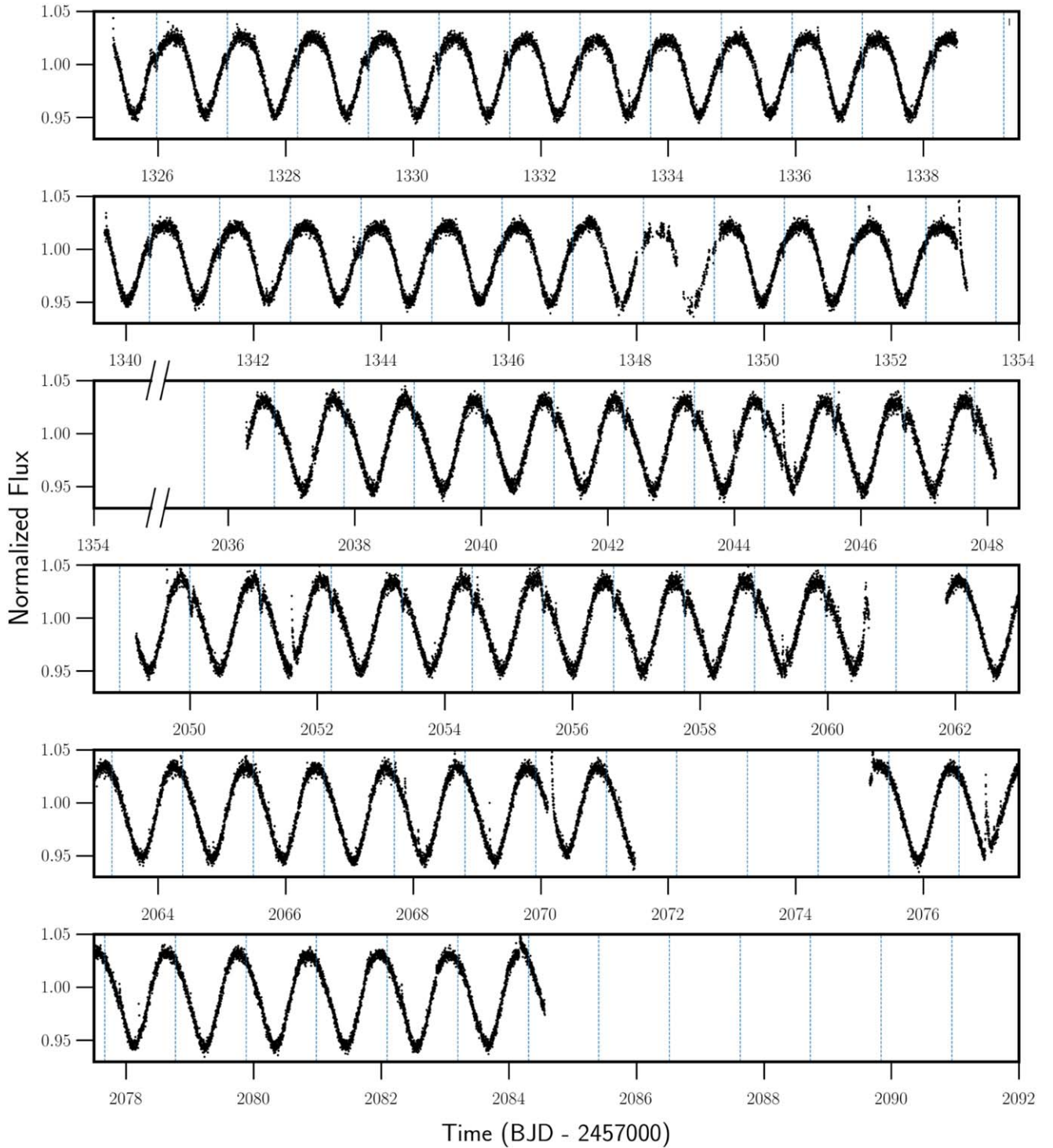


Figure 3. Two-minute cadence TESS data on TIC 234284556, with data and error bars in black. Dashed blue lines indicate the anticipated midpoint of each dimming event, projected forward using the rotational period of the star and the midpoint of the first dip in Sectors 1 and 27. The upper limit of the y-axis is held at a normalized flux of 1.05, so not all flares are visible in their entirety. The dip disappears quickly between days 2060 and 2062, consistent with centrifugal breakout.

the rotation removed, we detected a dip with an orbital period of 1.1065 ± 0.0037 days and a depth of $0.487 \pm 0.043\%$ over the sector. A closer investigation identified that the dip duration and depth vary gradually over the sector, ranging from 0.12% to 0.75% over the course of Sector 1. The overall trend is toward a decreasing dip depth over time, a phenomenon discussed in more detail in Section 6.2. The dip’s period is consistent with the 1.1071 ± 0.0036 day stellar rotation period

that we measured from the GP, suggesting a corotating object. Moreover, the shape of the event appears to be asymmetric, with a slower egress than ingress.

This system was re-observed by TESS in Sectors 27 and 28. In Sector 27, a very similar dip is apparent, although with a deeper depth, $0.756 \pm 0.043\%$ overall, with variation from 0.38% to 1.2% over the sector. We also see a change in phase and a reversal of the asymmetry, with the ingress now slower

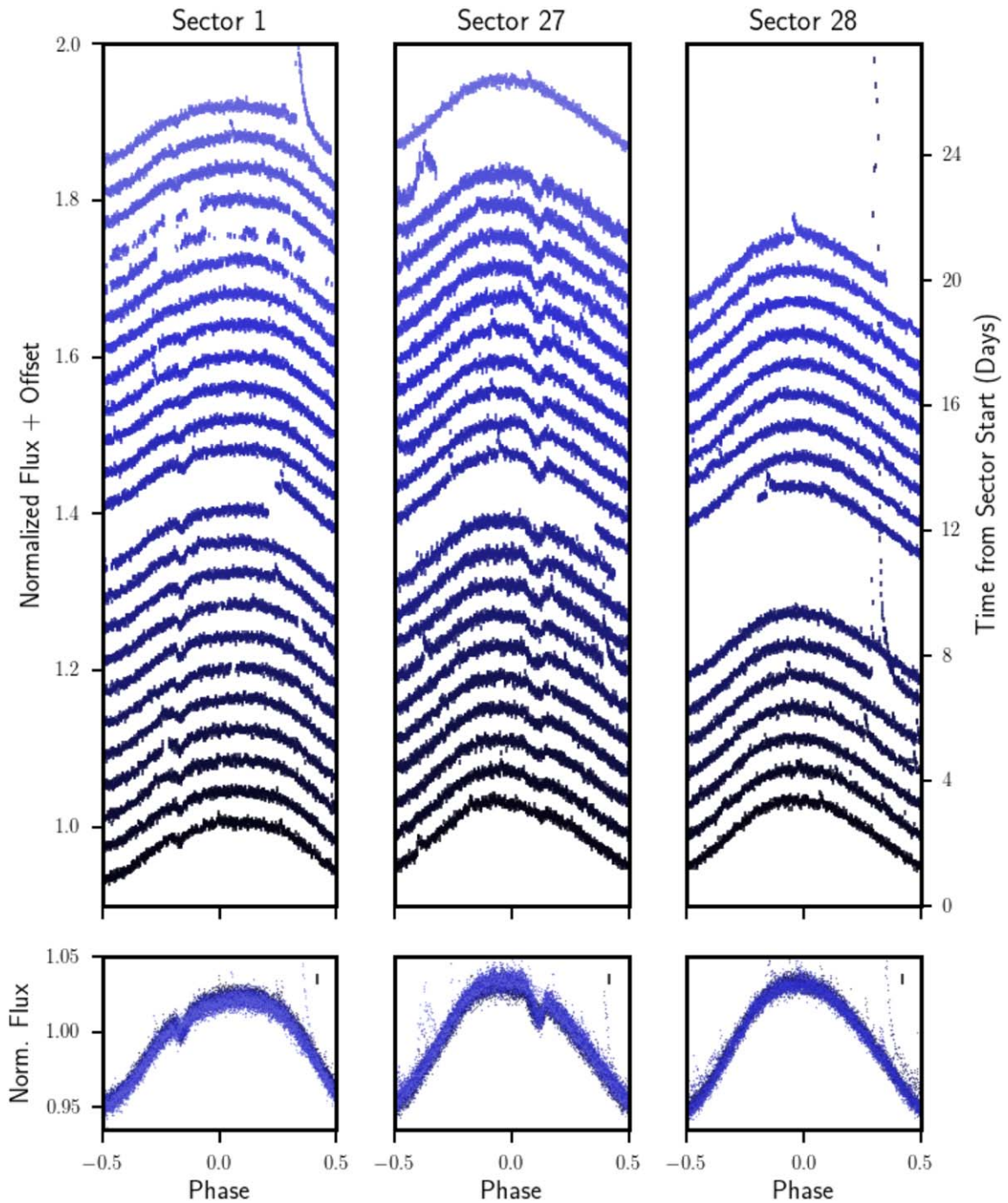


Figure 4. TESS light curve folded on the stellar rotation period. The observed dip evolves throughout Sectors 1 and 27, quickly disappearing between Sectors 27 and 28. An unusually symmetric flare-like brightening occurs at the very end of Sector 27, with a $> 120\%$ flare following some days later in Sector 28. A $+0.04$ vertical offset is added for each new rotational period, so that time progresses upward on the plot. To emphasize the short timescales involved, the first rotational period of Sector 28 is plotted in the Sector 27 panel.

than the egress, a phenomenon discussed in more detail in Section 3.2. Surprisingly, in Sector 28 there is no detectable periodic dip, even though it is separated from Sector 27 by only 1.2 days.

At a time that coincides with the rapid disappearance of the eclipse and immediately before the end of Sector 27, we see an anomalous brightening event with a morphology unlike the typical steep rise and exponential decay exhibited by a stellar flare (see the last partial orbit of Sector 27 in Figure 4). Although TESS data near the start and end of an orbit can have

significant systematics, this signal does not appear to be related to scattered Earthshine. Instead, we see similar behavior across the entire pixel response function, and neighboring stars do not exhibit such a feature, so we infer that the signal appears to be astrophysical and related to TIC 234284556.

TIC 234284556 has a strong and roughly sinusoidal rotational signature that is visible in Figures 3 and 4. In our final data analysis, we took advantage of this stable rotational signal to fit a ninth-degree polynomial to the folded, normalized light curve of the two-minute cadence data with the

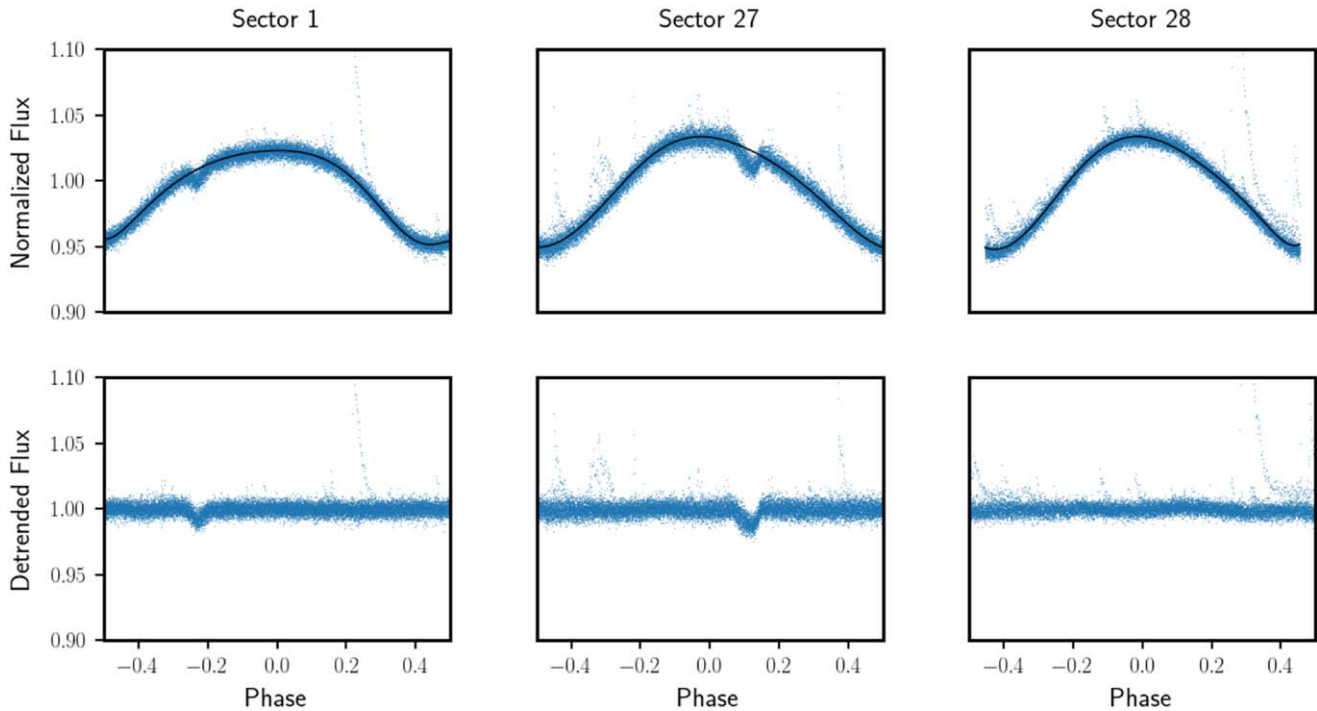


Figure 5. Detrending TESS light curves. Top panels: the normalized flux folded on the stellar rotation period is shown in blue with a ninth-degree polynomial fit to each sector in black. Bottom panels: the detrended, folded normalized flux, obtained by dividing the light curves from each sector by the corresponding ninth-degree polynomial. Note that the amplitude of the variability is larger in Sectors 27 and 28 than in Sector 1, an indicator of heightened magnetic activity around the time of the dip’s disappearance.

dimming events masked; the polynomial was created using `numpy.polyfit`. After repeating this process for each TESS sector, we divided our original data by a periodic version of this polynomial fit to obtain our detrended light curves, as shown in Figure 5.

2.3. All-Sky Automated Survey for Supernovae

TIC 234284556 was also observed by ASAS-SN (Shappee et al. 2014; Jayasinghe et al. 2021), with 208 data points collected over 4.4 yr, from 2014 May 12 to 2018 September 24 (HJD 2456789.859–2458385.597). There is overlap between the observations of TIC 234284556 during TESS Sector 1 and the ASAS-SN data. The uncertainties on and times between ASAS-SN’s measurements are too large for us to claim a detection of a dip during these additional four years of data. However, these data do confirm the stability of TIC 234284556’s rotational period and phase over timescales of years; in particular, the ASAS-SN database (Jayasinghe et al. 2021) reports a point estimate of 1.1066 days, which is consistent with the value that we measure from TESS.

While the period and phase are consistent over many years, the amplitude observed by ASAS-SN is not. We fit an individual sine wave with a fixed period but with amplitude, phase, and a constant offset as free parameters to the five years of ASAS-SN data and to the three sectors of TESS data. We find that the semi-amplitude of the signal in the ASAS-SN data varies from a minimum of $2.73 \pm 0.77\%$ in 2014 to a maximum of $7.45 \pm 0.60\%$ in 2016, as shown in Figure 6. Similarly, the semi-amplitude of the best-fit sinusoid to the TESS data varies from $3.726 \pm 0.007\%$ in Sector 1 to $4.261 \pm 0.008\%$ and $4.553 \pm 0.008\%$ in Sectors 27 and 28, respectively. These changes in the amplitude of the star’s variability

offer evidence for starspot evolution over the ASAS-SN and TESS baselines.

For a more precise estimate of the period of this rotational signal, we used the `lightkurve` (Lightkurve Collaboration et al. 2018) package’s Lomb–Scargle periodogram to find the maximum of the highest peak of the power spectrum of our star’s rotational signal. To produce this periodogram, we computed two separate power spectra, one for the ASAS-SN data and one with the TESS data to minimize aliases produced by their different cadences and observing strategies. After interpolating onto a linear grid, the product of these two power arrays produced the final periodogram, which is shown in Figure 7. Calculating the corresponding uncertainty using the FWHM of this peak of the power spectrum, we found our target star’s rotational period to be 1.1066 ± 0.0003 days, which is consistent with the 1.1071 ± 0.0036 day stellar rotational period that we inferred from the GP. This value is also consistent with the dip’s 1.1065 ± 0.0037 day orbital period.

2.4. Veloce–Rosso

We observed TIC 234284556 with the Veloce–Rosso spectrograph (Gilbert et al. 2018) at the 3.9-meter Anglo-Australian Telescope of the Siding Spring Observatory over six nights between 2020 October 27 and 2020 November 9. Veloce has a resolution of $R \approx 80,000$ and, at present, obtains data over the wavelength range 580–930 nm.

Because M dwarfs are dim red stars, the $H\alpha$ line is the most practical proxy for magnetic activity in their convective exteriors (Bell et al. 2012). Notably, stellar flares lead to heightened emission in the Balmer lines and other chromospheric spectral lines (Kowalski et al. 2013), and $H\alpha$ emission has also been associated with M dwarf activity–rotation

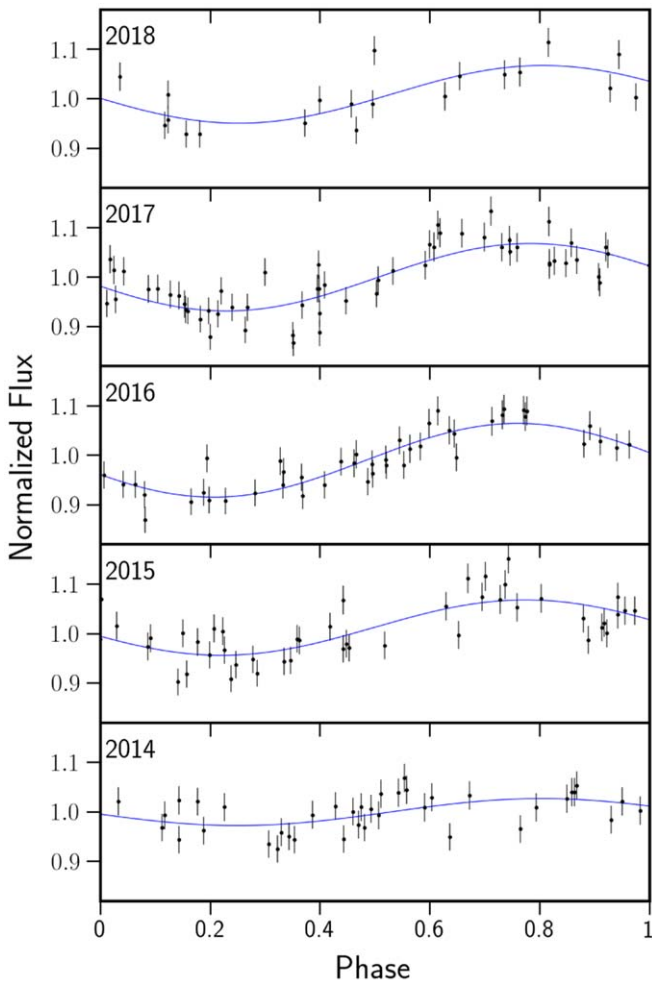


Figure 6. ASAS-SN data, labeled by year and shown with the best-fit sinusoid in blue. Note the variation in amplitude from year to year, with the semiamplitude ranging from $2.73 \pm 0.77\%$ in 2014 to $7.45 \pm 0.60\%$ in 2016. This variability indicates that the quasi-sinusoidal signal is driven by starspot evolution rather than an alternate mechanism such as Doppler beaming.

relations (Newton et al. 2017; Reiners et al. 2012). Accordingly, our analysis focuses on $H\alpha$, with the interpretation further discussed in Section 4.3.

Three of our exposures were taken as 20 minute observations; all other observations were 30 minutes in duration. We used the standard Veloce observing setup from its planet search program, similar to that of Bouma et al. (2020b). The air mass of these observations ranged from 1.18 to 1.49, while seeing ranged from $1''.7$ to $2''.8$. In total, we obtained 29 spectra. At wavelengths near $H\alpha$, the SNR of these spectra ranges from 10 to 27 per pixel with a mean SNR of 20.

We reduced these data to extract the spectral order containing the $H\alpha$ line. After removal of the bias level and flat field, we performed a box extraction over a region 49 pixels wide to account for the 19 target fibers corresponding to a $2''.5$ diameter region of the sky centered on our target. Veloce also obtains five sky spectra through offset fibers observed simultaneously, although we note that, at these wavelengths, the sky emission is negligible compared to the brightness of our target star. We infer a wavelength solution from observations of a thorium-xenon lamp with the same instrumental setup.

A significant $H\alpha$ emission signal, shown in Figure 8, is present in all 29 spectra obtained with Veloce. Equivalent widths vary over the range $W_\alpha = -7.8$ to -13.8 \AA , with the exception of three sequential spectra with $W_\alpha = -17.7$ to -18.2 \AA . These values are consistent with the $W_\alpha = -9.40 \text{ \AA}$ measured by Kraus et al. (2014) for this star and broadly fit with the range of equivalent widths measured by Kraus et al. (2014) for young M dwarfs in the Tuc–Hor association and by Scholz et al. (2007) for M dwarfs in the slightly younger β Pictoris moving group.

We fit a velocity-broadened template to Fe I lines near 840 nm to infer the projected rotational velocity of TIC 234284556, finding $V \sin i = 11.9 \pm 0.4 \text{ km s}^{-1}$. This value is consistent with the $11.9 \pm 0.9 \text{ km s}^{-1}$ velocity identified by Kraus et al. (2014). Combining this line width with the stellar rotational period inferred in Section 2.3, we derive an angle i_{rot} between TIC 234284556’s spin axis and TESS’s line of sight of $37.5 \pm 2.0^\circ$. We discuss the implications of this result in the context of the centrifugal breakout model in Section 4.4.

We also investigate the RV stability of these spectral features to place a limit on the mass of orbiting objects. We measure the centroid of individual Fe I lines across all epochs to infer a stellar radial velocity and fit the resultant RV signal to a sinusoidal signal with a period equal to that of the dips. This period is nearly identical to the stellar rotational period. Rotationally driven modulation of $\sim 100 \text{ m s}^{-1}$ has been observed in other members of Tuc–Hor (e.g., Montet et al. 2020), so while a detection would not unambiguously suggest a massive companion, we can place an upper limit on the potential mass of orbiting objects. Here, we can rule out signals with a 1.1 day period and a Doppler semiamplitude $K > 730 \text{ m s}^{-1}$ at 95% confidence. This constraint implies that if the observed dips are caused by a transiting object, its mass must be no larger than $2.1 M_{\text{Jup}}$.

2.5. Las Cumbres Observatory

We obtained follow-up time-series photometric observations of TIC 234284556 using the 1 m telescopes in the Las Cumbres Observatory network (LCO; Brown et al. 2013). The Sinistro cameras mounted on the LCO 1m telescopes have a $26' \times 26'$ field of view and an unbinned pixel scale of $0''.39 \text{ pix}^{-1}$.

The observations were conducted on the night of UT 2020 November 13 from the SAAO node, with mild defocusing. We opted to use the SDSS g' filter,¹¹ based on the expectation that the dips would be chromatic, with the largest depths in the bluest bandpasses (e.g., Onitsuka et al. 2017; Tanimoto et al. 2020; Günther et al. 2020a). Ingress and egress were predicted for 18:54 and 20:24 (UT) on the night of 2020 November 13 based on the TESS data. The observations began at astronomical dusk (UT 18:46), continuing until UT 20:53. The FWHM of the image point-spread function varied between 13.6 pix ($5''.2$) and 17.3 pix ($6''.7$), with a median value of 15.1 pix ($5''.9$).

We reduced the images to aperture photometry light curves using the FITSH package (Pál 2012), with the Gaia DR2 catalog used as a reference for determining the astrometric plate solution of each image. We used three concentric apertures for photometry with radii of 15 pix ($5''.8$), 20 pix ($7''.8$), and 25 pix ($9''.7$). The background flux was estimated in an annulus about

¹¹ http://svo2.cab.inta-csic.es/theory/fps/index.php?id=LasCumbres/LasCumbres.SDSS_gp&&mode=browse&gname=LasCumbres&gname2=LasCumbres#filter

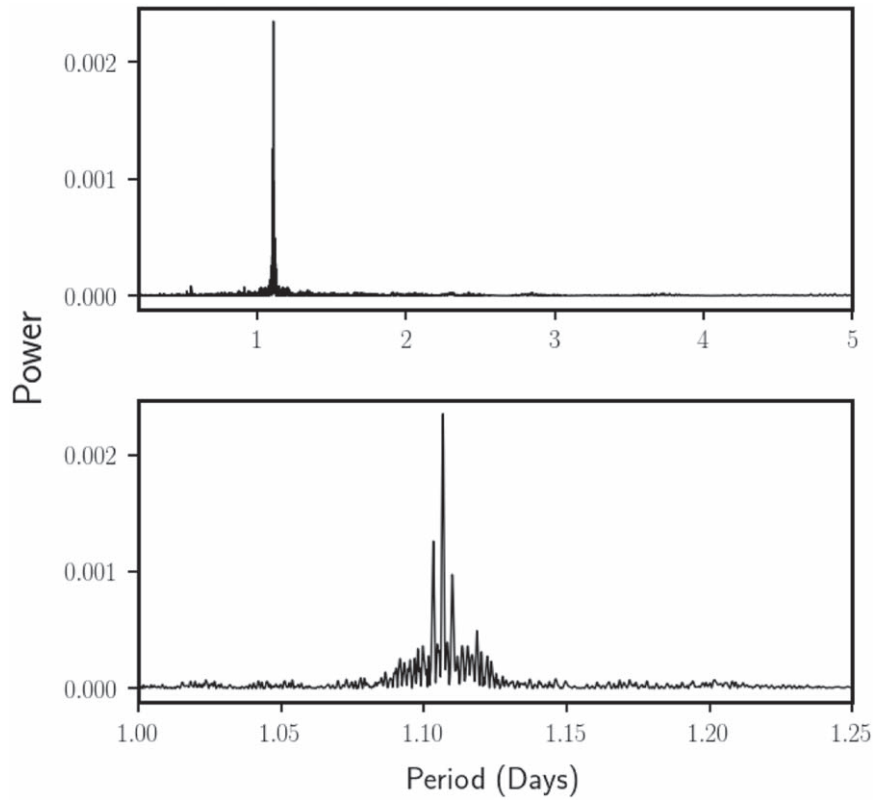


Figure 7. Power spectrum of TIC 234284556’s rotational signal, produced from TESS and ASAS-SN observations. We find that the star has a rotational period of 1.1066 ± 0.0003 days. This is consistent with the orbital period that we have established for the dip, suggesting that the orbiting material is nearly corotating.

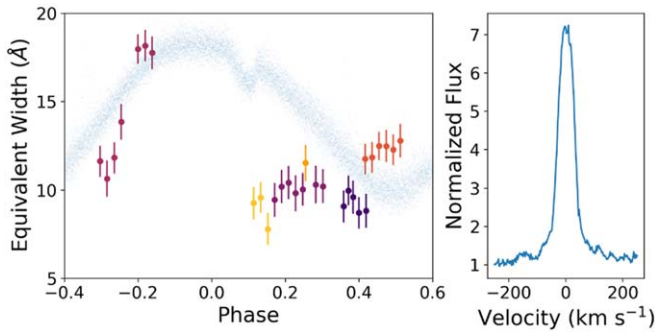


Figure 8. Velocero data. Left panel: the $H\alpha$ line’s equivalent width, with each color corresponding to a different day of observations, is plotted over the phased TESS data. Right panel: the $H\alpha$ signal, co-added across all observations.

each aperture with an inner radius of 51 pix ($19''.9$) and width of 20 pix ($7''.8$). For each aperture, the light curve of the target star had an ensemble correction applied using the other sources in the field as comparison stars. Auxiliary parameters, such as the image position, PSF shape, background, and background deviation were also measured, but given the uncertainty regarding the expected form for the astrophysical signal that would be present in the observations, we did not detrend against these parameters.

The results are shown in Figure 9. Here, a ~ 1 hr dip of depth ≈ 15 mmag appears at the beginning of the observing sequence. Fitting the dip to a transit model with the same shape as the Sector 27 events but with the depth allowed to vary as a free parameter, we measure a depth of $1.4 \pm 0.4\%$ in this filter. This event may not be associated with the Sector 27 event given the

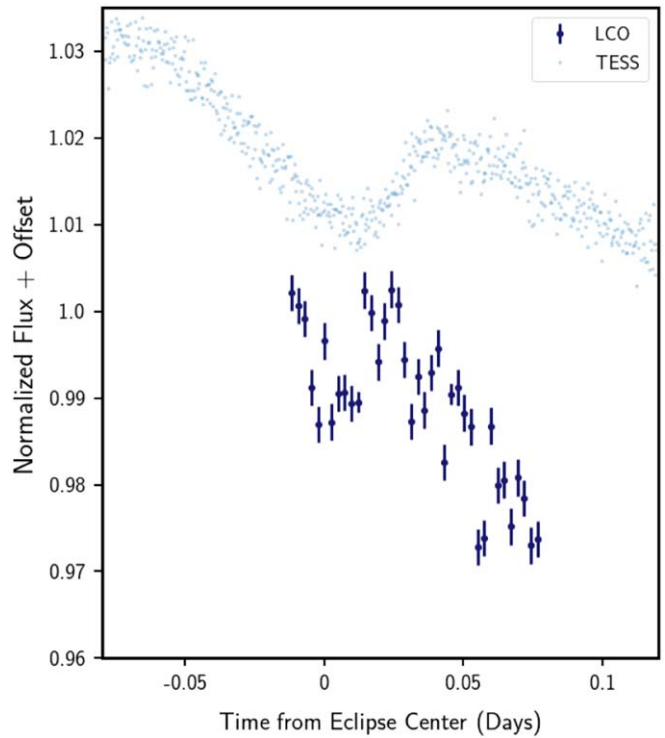


Figure 9. LCO follow-up photometry is shown in dark blue with Sector 27 TESS data from over 100 days earlier in light blue, providing evidence for the return of a dip over the intervening three months. An offset has been introduced between the two data sets’ flux values for ease of visualization. We interpret the different slope of the out-of-transit signal in the TESS and LCO data as reflecting observations in different bandpasses.

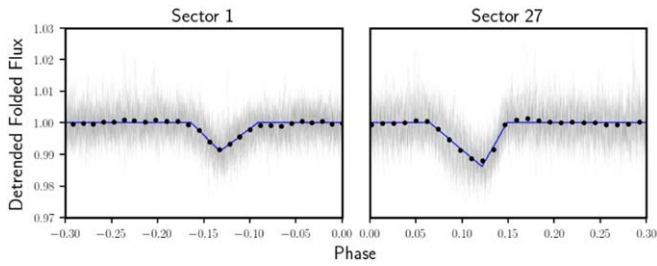


Figure 10. Asymmetry of TIC 234284556’s dips in Sectors 1 and 27. A section of the full detrended, folded TESS data, with error bars, is shown in gray. A binned version of this same data is shown in black. Our best-fit triangular transit model is superimposed in blue. Note the asymmetry of the transit, with the slower half of the event occurring on the side closest to the maximum brightness of the rotational modulation in both sectors.

Sector 28 nondetection. Moreover, since the opacity of the transiting material is likely to have a wavelength dependence, the different bandpasses of the two telescopes can produce apparent depth variations.

With those caveats in mind, we also considered a standard, symmetric transit model following the formalism of Mandel & Agol (2002), which produces a measured eclipse depth of $1.3 \pm 0.4\%$. Therefore, either set of assumptions produce a 3.5σ detection of a transit-like event on this night. The detection of this event is significant because the dip was not visible in TESS Sector 28, the last month of data collected prior to these LCO observations.

3. Analysis

3.1. Validating the Signal

In the TESS bandpass, TIC 234284556 is 7.3 magnitudes brighter than the closest star ($28''.92$; slightly larger than one TESS pixel) and 4 magnitudes brighter than any star within one arcminute. As four magnitudes corresponds to a flux ratio of 40, the rotational signal observed in both TESS and ASAS-SN data can only be attributed to TIC 234284556. If this signal were from a background star, it would require at least a 60% obscuration of that star to produce the diluted 1.5% dips observed in TESS data, and the periodic signals on two unassociated stars would need to have the same period to within 1–2 minutes, further underscoring the unlikely coincidence needed. Moreover, our LCO follow-up photometry indicates that the dips must be localized to the target star to within $\sim 2''$, well within the distance of any resolved sources in the Gaia EDR3 catalog (Gaia Collaboration et al. 2021), providing additional evidence that the signal indeed belongs to our target star.

3.2. Eclipse Profiles

TIC 234284556’s dips are visibly asymmetric, with a distinctively triangular shape (see Figure 10). To see the asymmetry more quantitatively, we individually performed a linear regression on the ingress and egress of the folded, detrended dips in both Sectors 1 and 27. We measured a slope for ingress and egress in Sector 1 of $-1.18 \pm 0.06\%$ per hour and $0.90 \pm 0.06\%$ per hour, respectively. In Sector 27, the measured slopes are $-1.008 \pm 0.025\%$ per hour and $2.11 \pm 0.07\%$ per hour, respectively. With both ingresses inconsistent with the absolute value of the slope of their

respective egresses, there is significant evidence for dip asymmetry in the TESS data.

It is especially interesting to compare these results with the eclipse features of RIK-210 and the transient flux-dip stars. Like TIC 234284556, those stars exhibit asymmetric and triangular transits (David et al. 2017; Stauffer et al. 2017). In particular, this triangular shape may be taken to suggest that the corotating material has a total extent roughly comparable to the size of their host star. Such a conclusion also matches David et al. (2017)’s estimates for RIK-210, which are based on the observed transit duration.

Interestingly, even with the phase change that occurred from Sectors 1 to 27, our dip is in both cases asymmetric in a similar way, with the shallower slope pointed to the peak of the starspot signal. An examination of light curves from other transient flux-dip stars indicates that they also seem to share this feature, hinting that there could be a physical mechanism—potentially related to the corotating plasma tracking magnetic activity—behind this feature. Future work will be needed to understand this in more detail.

3.3. Changes in Eclipse Parameters

The light curve shown in Figure 4 indicates that, apart from the sudden disappearance of the dip between Sector 27 and 28 (visible in the center panel), the variation in the depth and duration of TIC 234284556’s dips is systematic and gradual. As Figure 4 shows, we also see the signal shift in phase between Sectors 1 and 27, indicating either that the orbital period does not perfectly coincide with TIC 234284556’s rotational period or that the two signals have different origins.

We now analyze changes in the equivalent duration of the dips present around TIC 234284556. Following the methodology described in Hunt-Walker et al. (2012) for the analysis of stellar flares, but with opposite sign conventions, the equivalent duration t_{equiv} is defined by

$$t_{\text{equiv}} = \int_t (1 - F_{\text{norm}}) dt, \quad (3)$$

where F_{norm} is the normalized flux and the dips are integrated over all times t across their duration. This definition mirrors the equivalent width in spectroscopy, with an integral over time instead of wavelength. Conceptually, the equivalent duration expresses the amount of time that the star’s normalized flux would stay at zero in order for the same time-integrated amount of light to be blocked as in the actual event that we observe. Thus, the equivalent duration is a proxy for the amount of transiting material, and it is an appropriate choice for our purposes, since—as Figure 4 suggests—the duration, depth, and morphology of TIC 234284556’s dips change simultaneously.

To calculate the equivalent duration, we integrated across the dips in our detrended data from Sectors 1 and 27, using the median of the baseline immediately surrounding each dip for improved normalization. Results are shown in Figure 11 and indicate that variations in the equivalent duration are not purely stochastic, but rather vary systematically on ~ 20 day timescales. Moreover, as the center panel of Figure 4 indicates, we also see potential evidence of drift in the transiting material’s orbital period prior to the disappearance of the dip. However, as discussed in Section 5.3, dip duration and morphology changes

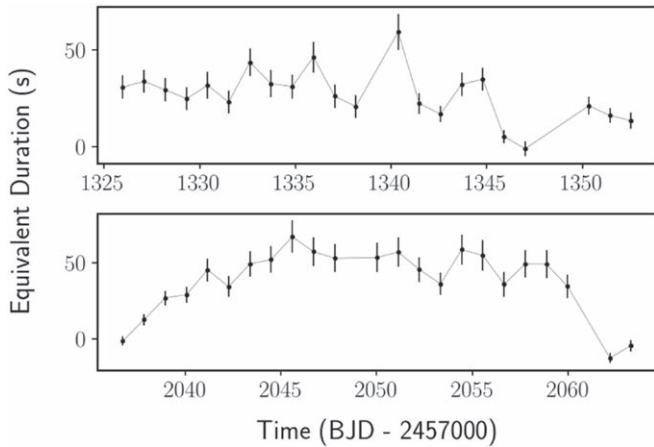


Figure 11. Changes in equivalent duration, the time-integrated observed flux decrement, and a proxy for the amount of material transiting the star during TESS Sectors 1 and 27. The first two orbits of Sector 28 are shown along with the Sector 27 data. Note the equivalent duration gradually decreases in Sector 1 and increases in Sector 27, followed by the sudden disappearance of any detectable dip between Sector 27 and 28.

are difficult to separate out from any possible drift, so we cannot be certain of this conclusion.

3.4. Flare Energies and Rate

To identify flares present in the light curve of TIC 234284556, we applied the convolutional neural network (CNN) *stella*, developed by Feinstein et al. (2020b) and trained on flares identified by Günther et al. (2020b). The *stella* CNNs allow for flare detection without removing underlying rotational modulation and assign probabilities to each identified flare being true. Following the methods of Feinstein et al. (2020b), we run and average the probability outputs of 10 CNN models. We included any flare with a *stella*-averaged probability >0.9 , which indicates the CNN models estimate a 90% confidence this is a true flare event. The result of this analysis is presented in Figure 12.

We identified 58 flares across all three TESS sectors, visible in Figures 4 and 12. The flare rate was calculated by weighting each flare by the probability assigned by *stella*, with an error bar assigned by assuming that flares follow a Poisson distribution. This yields an average flare rate of 1.35 ± 0.14 flares per day across Sectors 1, 27, and 28. Recent work from Howard et al. (2020) suggests that even 20,000 K flares may not be uncommon around low-mass stars, but we do not have any temperature information for individual flares given the single TESS bandpass. Here we assume a flare temperature of 9000 K, as is typical of flares around the Sun (Kretzschmar 2011). With this assumption, and taking T_{eff} for TIC 234284556 to be 3100 K, we find that the flares in the sample span an energy range of 1.6×10^{32} to 1.3×10^{34} erg, with a median energy of 9.4×10^{32} erg.

A triple-peaked flare event with an energy of 3.9×10^{35} erg and a measured equivalent duration of 1900.16 s was identified at $t=2070.128$ BTJD (Figure 13). A different flare was identified 16 minutes from the phase of the eclipse time projected from Sector 27, but there is no significant relation between the flare occurrence rate and phase overall, as shown in the bottom panel of Figure 12. Although geometric considerations can lead flares to be unobserved, we note that the observed flare rate is lower in Sector 1 (0.81 ± 0.17 flares

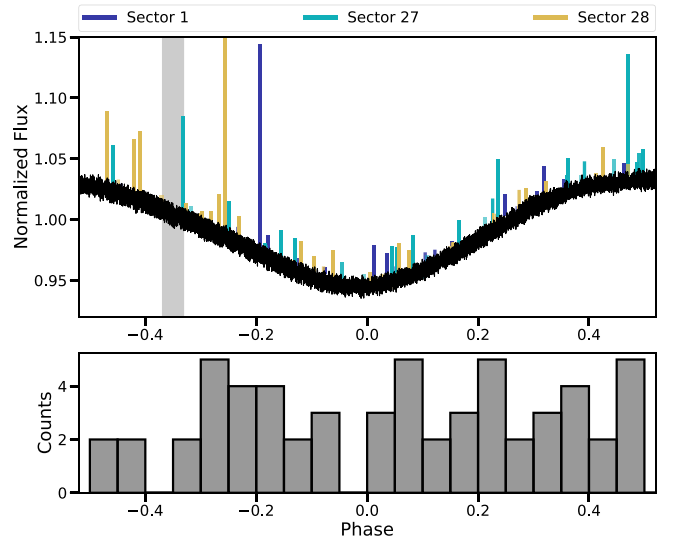


Figure 12. Results of the *stella* CNNs run on the three light curves of TIC 234284556. Top panel: distribution of flares over a phase-folded light curve for TIC 234284556. Flares are scaled by the amplitude of the flare and are colored by the TESS sector they were observed in. The gray shaded region highlights the phase at which the dip is located. The upper limit of the y-axis is held at a normalized flux of 1.15, so the largest flare in Sector 28, as shown in Figure 13, is not visible in its entirety. Bottom panel: a histogram representation of the number of flares identified at each rotational phase. Flares are binned in $\Delta \text{Phase} = 0.05$. There is no evidence for a correlation between flare rates and rotational phase.

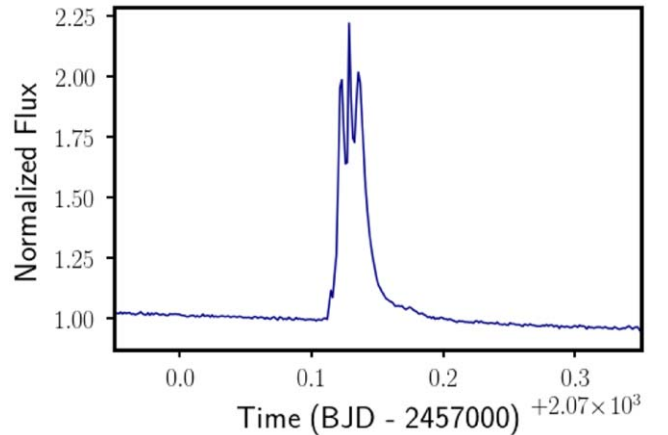


Figure 13. The $\approx 120\%$ triple flare in the TESS bandpass that appears in Sector 28, days after the disappearance of the dip. This may be interpreted as additional evidence for increased magnetic activity in the time surrounding the potential centrifugal breakout event.

per day) than in Sector 27 (1.45 ± 0.25 flares per day) and 28 (2.00 ± 0.32 flares per day). This quiescent period coincides with a period of relatively shallow dips, as further discussed in Section 6.2.

4. Potential Origins of the Eclipses

Here, we discuss possible origins of TIC 234284556's dips. We consider in turn the possibility that the dimming events are caused by a disintegrating or sublimating planet, a precessing planet, a planet transiting an active stellar surface, an eclipsing black-hole–M-dwarf binary, secondary eclipses of slingshot prominences, or transiting magnetospheric clouds, determining

that magnetospheric clouds are the most plausible cause of the dips.

4.1. A Planetary Origin

4.1.1. A Disintegrating or Sublimating Planet

A distinguishing feature of TIC 234284556’s light curve is the variation in its eclipse characteristics over a few days. Beyond the sudden disappearance of the dip over the course of one rotational period between Sectors 27 and 28, there are changes in the depth, duration, and morphology of the dips throughout Sectors 1 and 27 (See Figures 4 and 11).

There is precedent for changes in transit parameters in planetary systems. For example, variable mass loss by disintegrating planets can produce changes in the transit depth and duration (e.g., Sanchis-Ojeda et al. 2015; Vanderburg et al. 2015). However, the known disintegrating planets have somewhat shorter periods, ranging from 4.5 to 22 hr (Lieshout & Rappaport 2018, pp. 1–19; Vanderburg et al. 2015), more extreme and stochastic depth variations (Rappaport et al. 2012) and a pre- and/or postingress bump that may be ascribed to the scattering of light (Rappaport et al. 2012; Sanchis-Ojeda et al. 2015).

For this system orbiting a cool M dwarf, we conservatively estimate the Roche limit by assuming a low planet density, 0.5 g cm^{-3} . The Roche limit in this configuration is 0.0035 au, compared to a corotation radius of 0.016 au. Moreover, the gradual change in equivalent duration that we see in Figure 11 does not match the expectation for purely stochastic variations in the geometric arrangement of transiting dust. Based on these arguments, the dips in the light curve of TIC 234284556 are inconsistent with the presence of a disintegrating planet.

We next consider the possibility that the dips are instead caused by a sublimating planet. As in Section 2.1, we estimate the temperature of material at the Kepler corotation radius to be $T_K = 806 \pm 41 \text{ K}$. The transiting material is thus below the sublimation temperatures of olivine, pyroxene, and carbon, although likely above the sublimation temperature of iron (Kobayashi et al. 2011). This implies that the signal is likely not from the sublimation of a planet with an Earth-like composition, although a strictly iron core could, in principle, be sublimating. However, this scenario would not cleanly explain the corotation between the orbiting material and the stellar rotation or the phase change from Sector 1 to 27. Moreover, from Sector 28 data, we can rule out a dip deeper than 400 ppm, and therefore the presence of a planet bigger than $0.9 R_{\oplus}$, with 95% confidence. Hence, any material that we observe in Sector 27 is dominated by a component other than an opaque transiting planet, if one exists in the system.

4.1.2. A Precessing Planet

A precessing planet is a planet that is being torqued in and out of our line of sight by a massive object; this is another possible cause of the depth-varying dips that we observe, particularly since the dip disappears in TESS Sector 28. However, transits of precessing planets vary over timescales around two orders of magnitude larger than what is seen for TIC 234284556. For example, PTFO 8-8695, if explained as a transiting planet, is thought to have a precession period of 293 days or 581 days (Barnes et al. 2013). Meanwhile, K2-146, a mid-M dwarf with two transiting planets, shows extreme transit-timing variations and has an estimated nodal precession

period of 106 yr (Hamann et al. 2019). Since the dip disappears over a ~ 1 day timescale, precession alone cannot explain the sudden disappearance of the dip between Sectors 27 and 28. Additionally, a precessing planet does not neatly explain the match between the orbital and rotational periods or the phase change of the signal from Sectors 1 to 27.

4.1.3. A Planet Transiting an Active Stellar Surface

Another possibility is that the dips originate from a planet transiting an active latitude on TIC 234284556. Under this scenario, the planet’s transit chord would block a region on the stellar surface that has variable flux. For example, Sector 1’s gradual decrease in the dip depth over time could correspond to a planet that is transiting across a band of starspots, where that band is gradually growing to cover a larger fraction of the star’s surface over time; Sector 27’s increase in dip depth would then correspond to a decay of a similar band.

For this situation to explain the transit duration variations that we observe in Sectors 1 and 27, there would need to be a sharp boundary between the active region and the quiet region on the star. Otherwise, we would observe a dip that continues to have a consistent duration (due to the fixed size of the planet), despite varying depth during and between transits. Moreover, the gradual changes in dip equivalent duration that we observe (Figure 11) over the course of Sectors 1 and 27 imply that the active region must be moving slowly across the stellar surface. Finally, since we do not observe significant changes in the spot signal over the sector, the active band would likely have to be rotationally symmetric and therefore an active latitude.

However, the sudden disappearance of the dip at the Sector 27–28 boundary implies that this hypothetical active region would have to grow from a near-minimum state to its maximum state within a ~ 1 day timescale—at odds with the slow growth required to explain the changing dip parameters in Sectors 1 and 27. Moreover, given that we do not see any change in the rotational signal, this scenario would require that the rapid growth of the active latitude occurs uniformly, across all longitudes of the star. Long-term ASAS-SN data do not give any evidence for step-function magnitude changes at this level, so we can disfavor this model.

4.2. A Compact Companion

In principle, the stable and strong sinusoidal signal that we have, until now, attributed to TIC 234284556’s starspots could instead be explained by relativistic Doppler beaming. In this scenario, light emitted isotropically in a moving object’s reference frame becomes concentrated when moving toward an external observer and fainter when moving away, leading to an ellipsoidal modulation in the light curve (e.g., Mazeh & Faigler 2010; Faigler et al. 2013).

To first order, the amplitude of the beaming signal is proportional to $4K/c$, where K is the orbital Doppler semiamplitude and c the speed of light. In the context of our system, beaming would require TIC 234284556 to be a binary system with a black hole. Under this scenario, the transit-like signal would be caused by the secondary eclipse of TIC 234284556 by its compact companion, and the changing dip parameters could be explained due to varying levels of accretion onto the black hole.

We reject the compact companion hypothesis for two reasons. First, Doppler beaming would require an unchanging sinusoidal signal because the binary system would be expected to have fixed orbital parameters that would lead to a perfectly repeatable beaming effect. This is not, however, consistent with our observations. As described in Section 2.3, the observed amplitude varies by more than a factor of two from year to year, suggestive of starspot evolution and inconsistent with Doppler beaming.

Moreover, if TIC 234284556 were in a binary system, the semiamplitude of the photometric variability in the TESS data should correspond to a radial-velocity signal with an amplitude on the order of 2300 km s^{-1} , as inferred from Equation (2) from Loeb & Gaudi (2003) and accounting for bandpass effects after the methods of Herrero et al. (2014). We do not observe such variability in the spectra. This scenario would also require the black hole to have an implausibly large mass of over $1000 M_{\odot}$ (Loeb & Gaudi 2003). Hence, we can effectively rule out both the presence of a compact companion and this scenario for the origin of the dips.

4.3. Secondary Eclipses of Slingshot Prominences

Slingshot prominences are cool, dense, corotating clumps of gas that are trapped along coronal field lines (Jardine & Collier Cameron 2019). Prominences are especially common around stars with strong magnetic fields, such as young M dwarfs (Jardine & Collier Cameron 2019) like TIC 234284556. Importantly, the slingshot prominence model has an associated mass-balancing mechanism that is analogous to centrifugal breakout of trapped corotating material; we could potentially use such a mechanism to explain the sudden disappearance of the dip between TESS Sectors 27 and 28. According to the model presented in Jardine et al. (2020), slingshot prominences will continue to grow until the accumulated mass exceeds the limit of what the star’s magnetic field can constrain. At this point, the corotating material will be expelled.

In the slingshot prominence model, the dips are caused by corotating plasma that is emitting in specific spectral lines; when this plasma passes *behind* the star, there is a decrease in the flux that we observe. One prediction of this model would be extreme variations in the shape of $H\alpha$ as this plasma rotates across the stellar surface. These variations manifest themselves as changes in the line profile via the Rossiter–McLaughlin effect, as the blue-shifted and then red-shifted hemisphere of the rotating star is obscured in turn (Rossiter 1924; McLaughlin 1924).

However, our LCO data’s bandpass is bluer than 656 nm and therefore does not cover $H\alpha$. Moreover, the TESS bandpass is 4000 Å wide (Ricker et al. 2014) so the 5 Å change in equivalent width that Veloc observed (See Section 2.4) can only account for a 0.1% change in the flux—an order of magnitude smaller than the 1% dip that we observe. Accordingly, it seems that some other source of emissivity beyond $H\alpha$ is necessary to account for the observed depth of the dip under the slingshot prominence scenario. In analogy with David et al. (2017)’s reasoning for RIK-210, we conclude that Paschen-continuum bound-free emission could produce broadband dimmings of up to a few percent—deep enough to produce our observed dips around for TIC 234284556 although insufficient to explain RIK-210’s dimmings.

As described in Section 2.4, we observe a significant $H\alpha$ emission signal over all 29 spectra obtained with Veloc. The observed variability, shown in Figure 14, is largely coherent with the rotational modulation due to starspots, with a larger equivalent width observed when the starspot coverage in the visible hemisphere is higher. However, the seven observations from UT 2020 November 3 provide an exception to this trend. On this night, seven spectra were obtained: four spanning two hours and three additional spectra obtained after a 45 minute gap, spanning 90 minutes. The three spectra after the gap all exhibit an equivalent width in the $H\alpha$ line more than 20% larger than any other feature. Moreover, during these three exposures, the feature has an extended blue-shifted component with a velocity of $30\text{--}50 \text{ km s}^{-1}$.

This behavior is morphologically similar to spectroscopic signatures of flares (Honda et al. 2018; Maehara et al. 2021). In principle, it could also be emission from a corotating blue prominence; there is a gap of at least three days before and after these spectra were obtained. This would correspond to a shorter event timescale than those observed in Sectors 1 and 27 of TESS, but without simultaneous photometry, we cannot rule out this scenario.

However, given the high flare rate for this star and the lack of line profile variations in the core of the $H\alpha$ line for any spectra obtained over this 13 night baseline, we find a stellar flare to be the most plausible explanation of the increased equivalent width and blueward asymmetry on these nights. With that caveat, there is no significant change in the shape of the $H\alpha$ feature in time, a result that is counter to predictions for a slingshot prominence (e.g., Zaire et al. 2021). The stability of the shape of the $H\alpha$ line, which we would expect to be mirrored similar to that of the Paschen lines, thus suggests a different mechanism than the slingshot prominence model.

4.4. Transiting Magnetospheric Clouds

Like slingshot prominences, magnetospheric clouds consist of material originating from the star that gets trapped in the host star’s magnetosphere. However, the effects of eclipsing slingshot prominences would be primarily driven by hot plasma (Waugh et al. 2021), whereas transiting magnetospheric clouds trap dust as well as ionized hydrogen, leading to additional opacity visible in broadband photometry (e.g., David et al. 2017). Since only a small amount of dust is needed to create significant optical dimmings, a magnetospheric cloud’s photometric signature can occur during a transit rather than during a secondary eclipse.

As with slingshot prominences, magnetospheric clouds would produce a signal with a period matching the rotational period. As material fills and seeps out of the magnetically confined region of material, the depth of the eclipses can vary over time. As the material is gas and dust grains, it will have a relatively weak wavelength dependence compared to the strong spectral signature of a plasma in the slingshot prominence scenario. These predictions match the variable light curve and unchanging line profile variations observed in this data set, making this scenario our preferred explanation for the observed behavior of TIC 234284556.

For RIK-210, a potential younger analog of TIC 234284556, David et al. (2017) also preferred the magnetospheric cloud model over the slingshot prominence model, finding that

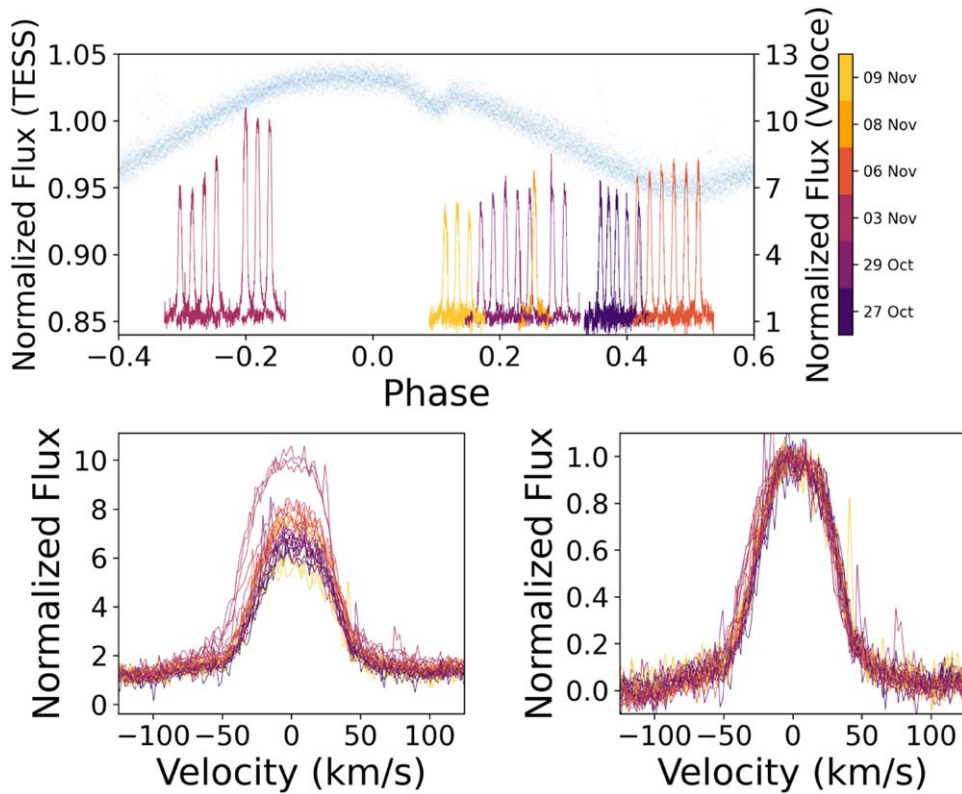


Figure 14. Top panel: phase-folded light curve for Sector 27, with normalized H α spectra plotted at the phases of observations. Bottom left panel: the same H α spectra, overplotted. There are no significant shape variations over this spectral feature, leading us to disfavor the eclipsing slingshot prominence scenario. For both frames, colors correspond to the night of observation, as indicated by the color bar on the right. The amplitude of this feature varies with starspot coverage, as is typical for young stars. There are three spectra, observed sequentially, with significantly larger amplitudes and excess emission at blue wavelengths compared to all other observations; we attribute this variability to a potential flare event on this star during these observations. Bottom right panel: the same as the previous figure, with all spectra excluding the three belonging to the flare candidate normalized to the same amplitude and equivalent width to demonstrate no significant shape variations over the remaining observations. Since the shape of the H α signal is very stable, the equivalent width maps consistently to the height of the spectral line, we exclude it to avoid redundancy.

eclipses of prominences could not explain RIK-210’s 20% deep dips in the Kepler bandpass. Although the dip depth of TIC 234284556 ($\leq 1.2\%$) is not large enough to conclusively rule out the slingshot prominence scenario on these grounds, the observed lack of variability in the H α line profile still gives us reason to prefer the magnetospheric cloud scenario over the slingshot prominence model.

Simulations from Townsend (2008) demonstrate that a signal similar to the eclipse events that we observe around TIC 234284556 can be produced with an inclination angle $i_{\text{rot}} \approx 40^\circ$ and a magnetic obliquity—the angle between the star’s spin axis and magnetic field axis— $\beta \approx 70^\circ\text{--}80^\circ$. These models are not specific to a star with TIC 234284556’s radius and rotational period, so the simulated inclinations and obliquities may not translate exactly to predictions for TIC 234284556. However, they do match the observed inclination value of $i = 37.5 \pm 2.0$ from TIC 234284556’s radius, projected rotational velocity, and rotation period, providing confidence that relatively low inclinations and high obliquities can produce light curves morphologically similar to those collected by TESS.

If the signal observed in this system is indeed the result of magnetospheric clouds, then we require an explanation of how sufficient material can become trapped in the magnetosphere of TIC 234284556 and of how this material can dissipate over the 1–2 rotation periods between Sectors 27 and 28. These are discussed in turn below.

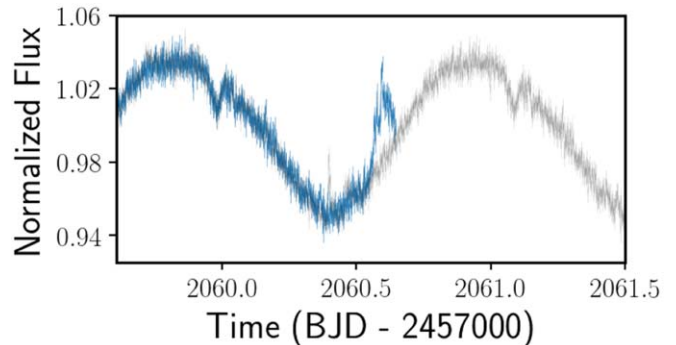


Figure 15. TESS light curve at the end of Sector 27 (blue), with an observed brightening at the end of the sector. For comparison, the light curve from one rotational period earlier is underlaid (gray). Note that this brightening event has a symmetric morphology unlike the steep rise and exponential decline typical of stellar flares. We consider this feature a potential postbreakout magnetic reconnection event, highlighting that the potential analogs of TIC 234284556 discussed in Stauffer et al. (2017) also exhibited symmetric flare-like events at state transitions.

5. Centrifugal Breakout

5.1. The Case for Breakout

Perhaps the most distinguishing feature of TIC 234284556’s dips is their sudden disappearance over a ~ 1 day timescale. Immediately prior to the disappearance of the dip, we observe a flare-like event with an unusually symmetric morphology (see

Figure 15 and Section 2.2). Moreover, in the days surrounding the dip’s disappearance, we see additional evidence for increased magnetic activity, including a $\approx 120\%$ triple flare some days after the potential breakout event (Figure 13) as well as a higher amplitude variability of the starspot signal in Sectors 27 and 28 as compared to Sector 1 (Figures 4 and 5). In addition to the dip’s sudden disappearance, we also see evidence of variability on top of a rotational signal that is strong and stable over timescales of years. In particular, we see systematic variations in the equivalent duration of TIC 234284556’s eclipses (see Figure 11 and Section 3.3), a phase change of the seemingly corotating dip from Sectors 1 to 27, and a reappearance of the dip in our LCO data.

All of these data are consistent with a magnetospheric cloud and centrifugal breakout model. The short timescale involved in the dip’s disappearance is plausibly explained by a sudden snapping of the star’s magnetic field lines when the mass of the corotating material exceeds TIC 234284556’s capacity to restrain it, whereas the alternative mass-balancing mechanisms discussed in Section 6.2 would predict longer timescales. Meanwhile, the heightened magnetic activity around the time of the dip’s disappearance would also be expected from centrifugal breakout and the unusually symmetric flare-like event that coincides with the dip’s disappearance (Figure 15) could plausibly be a postbreakout magnetic reconnection event.

In support of this last point, the existing theories of stellar magnetism predict that magnetic reconnection events could resemble flares (Townsend et al. 2013; Stauffer et al. 2017), although a link between optical flaring and reconnection events specific to centrifugally supported magnetospheres has yet to be definitively established (Townsend et al. 2013). Interestingly, like TIC 234284556, some of the persistent flux-dip stars and scallop shell stars had unusually symmetric flare-like events that occurred at state transitions (Stauffer et al. 2017). Since these state transitions and the corotating cloud origin promoted by Stauffer et al. (2017, 2018, 2021) fit many of the same criteria for centrifugal breakout that TIC 234284556 does, this correlation between symmetric flares and major changes in the dip properties could be taken to be an indication of the magnetic reconnection events that are expected to occur immediately after the magnetic field lines are broken during a breakout event.

Moreover, the physical mechanism of centrifugal breakout fits with the magnetospheric cloud dip origin that Section 4 found to be the most probable, and TIC 234284556’s rotational signature, spectral type, and youth suggest that the star does, in fact, likely have a strong and stable magnetic field—one of the prerequisites for a corotating magnetosphere. Furthermore, the systematic variations observed in the equivalent duration of TIC 234284556’s transit-like events (See Figure 11 and Section 3.3) is one of the indicators of breakout that Townsend et al. (2013) sought in their nondetection of centrifugal breakout around σ Ori E. Finally, a comparison with Morin et al. (2010) suggests that the magnetic field topology of the star could plausibly have evolved over the TESS baseline, leading to the change in dip phase observed between Sectors 1 and 27. Alternatively, the phase change could be attributed to anisotropic mass loss from coronal mass ejections, as further discussed in Section 6.2.

Regardless of the cause of the phase change, centrifugal breakout of magnetospheric clouds provides the most compelling explanation for the sudden disappearance of the observed

dip. This is the only model of the possibilities considered in this work that can fully explain the observations and that matches theoretical predictions of an expected signal (here, Townsend 2008).

5.2. Constraining the Prebreakout Mass

Appendix A2 of Townsend & Owocki (2005) estimates the asymptotic mass, or mass required for breakout to occur, as

$$m_\infty \approx \frac{\sqrt{\pi} B_*^2 R_*^4}{6 g_* r_K^2}, \quad (4)$$

where B_* is the strength of the star’s magnetic field, R_* is the radius of the star, and g_* is the star’s surface gravity, and r_K is the Kepler corotation radius.

In the absence of direct measurements of TIC 234284556’s magnetic field strength, we note that observations by Shulyak et al. (2019) would predict a magnetic field strength of around 4 ± 2 kG for an M dwarf with TIC 234284556’s rotational period. Accordingly, we tentatively take $B_* = 4$ kG for an order of magnitude estimate of TIC 234284556’s magnetic field strength. Using this value together with the stellar parameters listed in Table 2 and Equations (4) and (1), we find the asymptotic mass to be only $\sim 10^{21}$ g, which is about half the mass of Saturn’s satellite Janus and eight orders of magnitude below the upper limits given by the observed SED (Section 2.1). This demonstrates that only a small amount of mass is needed to reach breakout conditions. This material may originate from the last remnants of a dissipating protoplanetary disk and could potentially be replenished by material falling off of young objects—such as comets or forming planets.

It is also a useful exercise to compare the theoretically predicted asymptotic mass with the mass that we would expect based on the observed depth of the dip immediately prior to breakout. Here we use an approach inspired by Boyajian et al. (2016) to estimate a lower limit for the mass of dust present immediately before the possible breakout event from the depth of the dip. We then make an order of magnitude approximation of the total minimum mass of transiting material, based on our observational lower bound on the mass of optically thick material.

First, Equation (4) from Boyajian et al. (2016) gives

$$\sigma_{\text{tot}} = v_t h \int \tau(t) dt \quad (5)$$

to estimate the cross sectional area σ_{tot} of the optically thick corotating material. Here, v_t is the transverse velocity of the material, h the height of the material perpendicular to its velocity, and $\tau(t)$ the optical depth as it changes over the course of a rotational period.

For h , we assume a spherical shape for the corotating material and use 1.2% as the approximate depth of the last dip in Sector 27. For v_t , we assume uniform circular motion so that $v_t = 2\pi r_K / P$, where P , the orbital period of the material, coincides with TIC 234284556’s rotational period and the orbital radius of the material is the Kepler corotation radius. Finally, to approximate $\int \tau(t) dt$ for the dip immediately prior to breakout, we use the approximation that $\tau \approx \ln(\text{normalized flux})$. We detrend the normalized light curve as described in Section 2.2 and then integrate numerically over the dip. In this way we find that $\sigma_{\text{tot}} = 4 \times 10^{14} \text{ m}^2$.

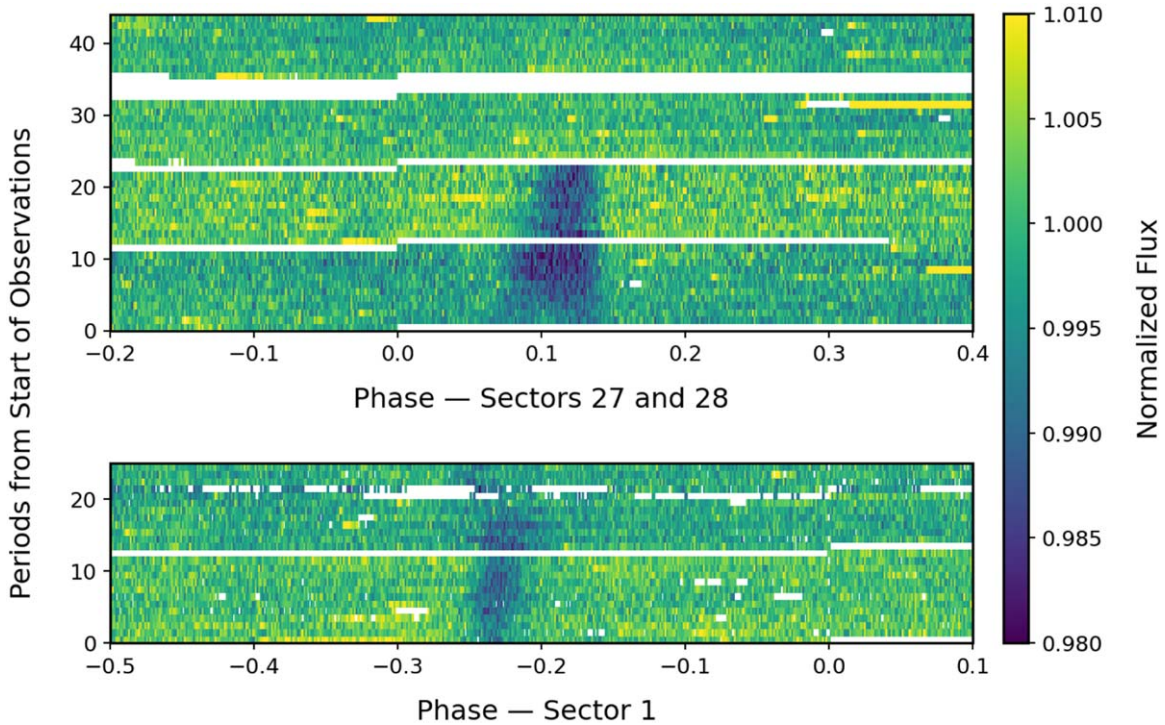


Figure 16. River plot of TESS data phased to the stellar spin period of 1.1066 days and with the rotational signal removed. There is an observed drift of the transit midpoint and the transit duration changes from event to event. The sudden disappearance of the dip between Sectors 27 and 28, which corresponds to the potential breakout event, is also apparent.

As in Boyajian et al. (2016), we calculate a lower limit for the mass of dust transiting the star that is given by

$$M_p = \frac{2}{3} \sigma_{\text{tot}} \rho D, \quad (6)$$

where we take the dust grains to be made of particles with a uniform density $\rho = 3 \text{ g cm}^{-3}$ and diameter $D = 1 \text{ }\mu\text{m}$.

In this way, we would obtain an equivalent radius of 400 m if all of the dust were gathered into a sphere with density 3 g cm^{-3} , and we estimate a dust mass of $9 \times 10^{14} \text{ g}$. If we assume a typical 100:1 gas-to-dust ratio in protoplanetary disks, this gives us a minimum mass of $9 \times 10^{16} \text{ g}$ —about a quarter the mass of Halley’s comet—for all of the transiting material.

This value is four orders of magnitude below the asymptotic mass calculated above. However, in producing the observation-based minimum mass, we have assumed that we see the entire cloud transiting, and we also do not have well-constrained estimates for the spatial distribution, diameter, composition, and density of the transiting material. Similarly, in the previous calculation, we do not have a precise measurement of the magnetic field; as the mass scales as B_*^2 this is a large source of uncertainty. Hence the disagreement between observation and theory suggests that either we are only seeing a small fraction of the plasma transit, the stellar magnetic field is lower than expected, or the true dust mass fraction is lower than predicted. Future work will be needed to fully explain this discrepancy.

5.3. Asynchronicity of the Signal

So far, we have presented the transiting material as likely to be corotating with the star. After all, the period of TIC 234284556 falls within our one sigma confidence interval for the period of the dip. However, as Figure 16, a river plot of

the three sectors of TESS data, shows, the transit midpoint appears to start falling behind the predicted ephemeris as time goes on. It is not clear if this apparent drift is best explained by a change in dip duration or by a genuine change in the orbital period. In fact, even as the ingress and transit midpoint in Sector 27 begin to lag, the egress remains at a relatively constant phase throughout the sector.

If we take this apparent drift at face value, this would correspond to 16 minutes of drift over the course of Sector 27, with a similar, though less pronounced, phenomenon occurring during Sector 1. This corresponds to a difference of less than one minute between the rotational and orbital periods. In the context of centrifugal breakout, such a drift in period could be interpreted as evidence of material gradually drifting outwards and dragging the magnetic field lines behind it until the field lines snap at the time of a breakout event. However, once again, dip duration and morphology changes are difficult to separate out from any possible drift, so we cannot be certain of this conclusion.

6. Discussion

6.1. Toward Timescale Estimates

The evolution of TIC 234284556’s dips appears to be governed by changes occurring on three different timescales:

1. The disappearance of the dip, which, for TIC 234284556, occurs on a ~ 1 day timescale.
2. Changes in the depth, duration, and shape of the dip, seemingly on a ~ 10 day timescale.
3. The postbreakout reappearance of the dip, poorly constrained by our current data, but occurring no more slowly than on ~ 100 day timescales.

In particular, we suspect that our current data on TIC 234284556 corresponds to a minimum of three distinct dips, with one change inferred from the shift in the phase of the corotating plasma from Sectors 1 to 27, and another from the dip detected in the LCO data 107 days after the dip disappeared between Sectors 27 and 28. Importantly, we have no lower bound on the timescales involved in the postbreakout reappearance of the dip—and we would need such information in order to distinguish between the CME and stellar wind mass-accumulation scenarios that are presented in Section 6.3.2.

The timescales for the disappearance of the dip and for the dip depth, duration, and morphological changes appears to be broadly consistent with those for the transient flux-dip stars from Stauffer et al. (2017). Notably, however, for TIC 234284556 we have a two-year baseline over which the dips are observed, which is important for understanding the longer-term evolution of this type of star. In particular, in these two years of data, we see a phase change, with the dip in Sector 27 offset in phase from the dip in Sector 1 by 29% of an orbit—something observed in PTFO 8-8695 and TIC 234284556, but not in any of the other known transient flux-dip stars.

6.2. Mass-balancing Mechanisms

Since Townsend et al. (2013) found a lack of photometric evidence for centrifugal breakout around σ Ori E, astronomers have been considering alternate mass-balancing mechanisms for plasma accumulating in a centrifugal magnetosphere. In particular, Owocki & Cranmer (2018) presented a diffusion-drift model in which plasma escapes away from the star via diffusion and drift, and toward the star via diffusion. Shultz et al. (2020), after examining early-B stars with confirmed centrifugal magnetospheres and finding that their $H\alpha$ emission profiles favor centrifugal breakout over the diffusion and drift model, proposed that centrifugal breakout is the relevant mass-balancing mechanism, but that it essentially acts as a leakage mechanism.

Meanwhile, Owocki et al. (2020) provided an analytical framework for analyzing the observations of Shultz et al. (2020). In particular, Owocki et al. (2020) proposed two possible explanations for the sudden onset of $H\alpha$ emission in early- to mid-B-type stars observed by Shultz et al. (2020). In one explanation, the diffusion-drift model is still an important mechanism for late-B and A-type stars because the much weaker winds of these less massive stars would not allow their centrifugal magnetospheres to fill the level needed for breakout. Alternatively, stellar winds may become dominated by metal ions around stars later than mid-B and therefore lack the hydrogen needed for $H\alpha$ emission.

We argue that TIC 234284556 provides strong supporting evidence for the centrifugal breakout model, with its light curve complementing the spectroscopic and theoretical case for this model. Moreover, TIC 234284556 seems to belong to the same class of stars as PTFO 8-8695 and those studied in Stauffer et al. (2017), suggesting that some of the observable features of these light curves, such as the state changes and phase changes, may also be driven by the centrifugal breakout mechanism. In particular, considering the sudden disappearance of the dip around TIC 234284556, the centrifugal breakout candidate that we observe cannot be governed by purely continuous centrifugal leakage of the kind proposed by Shultz et al. (2020).

However, centrifugal breakout alone does not explain the gradual decrease in dip size observed in Sector 1, suggesting

that there may still be a role for an additional mass-balancing mechanism. Although we cannot exclude a centrifugal leakage-based explanation, we consider that the corotating material will only interact with the stellar magnetic field when the dust is hot enough to stay ionized.

The dust will remain ionized while stellar flares continue to heat the corotating material. However, if TIC 234284556 enters a quiescent period, the dust will begin to undergo recombination and the apparent dip will decay. This flaring mechanism seems plausible because the work function of circumstellar dust is on the order of ~ 5 eV (Tielens 2005), so the UV radiation from flares provides sufficient energy to maintain dust in a state of ionization. This mechanism is discussed further by Osten et al. (2013).

In the context of TIC 234284556, we note a lack of major flares in the last several days of Sector 1 (see Figures 12 and 17). The decay in dip size throughout the second orbit of Sector 1 is qualitatively consistent with the model proposed here. In fact, the shallowest observed eclipse in Sector 1 occurs immediately after the 10 day period with the lowest flare rate in Sector 1 and 27; similarly, the flare energy per cycle is noticeably elevated in the days surrounding the deepest dips toward the end of Sector 27 (Figure 17). Finally, there is an observed correlation (Spearman $\rho = 0.317$) between the integrated flare energy observed and the measured equivalent duration of each dip across Sectors 1 and 27, hinting at the possibility of a connection between these two observables.

6.3. Comparison with Higher-mass Stars

6.3.1. Mass Dependence of Magnetic Fields

Townsend & Owocki (2005) developed the RRM model that predicted centrifugal breakout for high-mass stars like the B2 σ Ori E, but TIC 234284556 is an M dwarf. Nevertheless, the three main prerequisites for applying the RRM model, a (1) strong (kG), (2) globally organized, and (3) stable magnetic field, can be replicated with an M-dwarf magnetic field.

Around magnetic hot stars, the minimum field strength for a stable, large-scale magnetic field appears to occur around 300 G (Aurière et al. 2007), with stars like σ Ori E having field strengths of several kG (e.g., Oksala et al. 2015). Similarly, observations by Shulyak et al. (2019) would predict a magnetic field strength of 4 ± 2 kG for a rapidly rotating M dwarf like TIC 234284556.

Moreover, magnetic A- and B-type stars often have simple magnetic fields with a globally dipole structure (Briquet 2015). Although it is common for low-mass stars to have a complex magnetic topology (e.g., Hubrig & Schöller 2019), mid-M dwarfs often have strong, axisymmetric, dipole-dominated magnetic field configurations (Kochukhov 2021). Although future tomography observations could place tighter constraints on its spot configuration, based on its light curve, TIC 234284556 appears to have a single or small number of large spot groups (Basri & Nguyen 2018), similar to the spot coverage that would be expected from a star with a globally organized dipolar field (Shulyak et al. 2019).

As for stability, magnetic hot stars are thought to have “fossil” magnetic fields that were generated early in their lifetime and that naturally exhibit almost no variability, even over decades (Donati & Landstreet 2009). Although cool stars’ deep convective zones allow for field-generating currents that maintain magnetic fields through dynamo processes and that

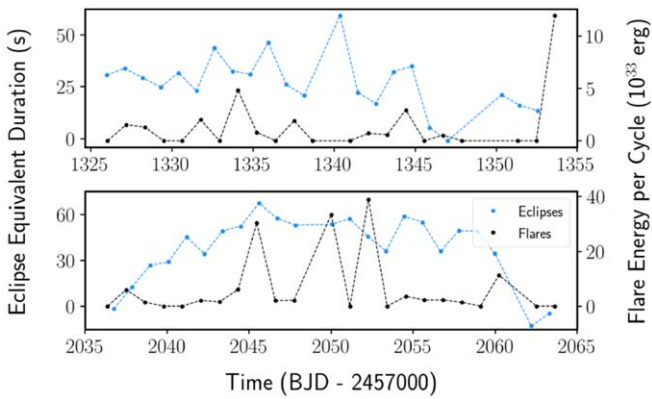


Figure 17. Equivalent durations and flare energies in TESS Sectors 1 (top panel) and 27 (bottom panel). Blue: dip equivalent durations, as calculated in Section 3.3. Black: an estimate for the total observed flare energy released in the preceding rotational cycle, calculated using flare events identified in Section 3.4. Note the low flare energy in the days before the dip in Sector 1 fades away and the high flare energy surrounding the days in Sector 27 when the dip is near its deepest. Importantly, both of these observations are consistent with the flare-based reionization mechanism that we propose is responsible for the gradual fading of the dip in Sector 1.

lead to noticeable variability (for example, flares and activity cycles) on both short and long timescales (Donati & Landstreet 2009), M dwarfs too can have magnetic fields that are stable for over a decade. GJ 1243 is one notable example (Davenport et al. 2020). In the case of TIC 234284556, the fact that the rotational phase is consistent over both ASAS-SN and TESS data shows us that its starspot configuration—and by implication its magnetic field—appears to remain stable for at least 6 yr.

All things considered, despite their different origins and activity levels, it appears that TIC 234284556 and a broader class of M dwarfs share with B-type stars the properties that are essential to applications of the RRM model. These similarities cast doubt on the interpretation that a different magnetic field structure is responsible for setting apart centrifugal leakage around high-mass stars and centrifugal breakout around low-mass stars. Accordingly, we now turn to an alternative explanation.

6.3.2. Stellar Winds or CME?

For massive stars, the stellar wind is typically considered as the primary source of the plasma trapped in their centrifugal magnetospheres (Townsend & Owocki 2005; Shultz et al. 2020), but an M dwarf’s stellar wind may not supply enough material for the asymptotic mass to be reached. For low-mass stars, the mass-loss rates from stellar wind \dot{M}_{wind} are very difficult to constrain: estimates in the literature differ by nearly five orders of magnitude from $4 \times 10^{-15} M_{\odot} \text{ yr}^{-1}$ to $10^{-10} M_{\odot} \text{ yr}^{-1}$ (Vidotto et al. 2014a).

In recent years, it has been suggested that, among young stars, the mass-loss from CMEs \dot{M}_{CME} may dominate over the outflow from the stellar wind (Jardine & Collier Cameron 2019), possibly by one to two orders of magnitude, for solar-mass stars younger than 300 Myr (Cranmer 2017). Even more interesting, Alvarado-Gómez et al. (2018)’s simulations of low-mass star CMEs indicated that a strong dipolar magnetic field prevents CMEs from breaking free from their stars, albeit with models developed for slowly rotating stars. All of this raises the question of whether a different

mass-feeding mechanism—stellar winds for high-mass stars, coronal mass ejections for low-mass stars—could explain the evidence that favors centrifugal leakage for hot stars but centrifugal breakout for low-mass ones.

Moreover, for high-mass stars, the magnetosphere would be steadily fed by an isotropic wind, with a high-mass star’s perfectly stable fossil magnetic field in the background. This, in turn, would allow the breakout rate to match \dot{M}_{wind} , leading high-mass stars to exhibit the continuous form of centrifugal breakout that Shultz et al. (2020) introduced as “centrifugal leakage.” Stochastic CMEs, by contrast, would lead to impulsive, localized mass feeding and the low-mass star’s dynamo-generated magnetic field would only be quasi-stable. Accordingly, the asymptotic mass could be reached by the expulsion of a CME, by the gradual feeding of the wind, or by a reorganization of the background magnetic field due to normal dynamo action (e.g., Morin et al. 2010). Under this scenario, centrifugal breakout events could occur suddenly and unpredictably, mirroring the magnetic activity that causes them.

The lack of evidence for centrifugal breakout around high-mass stars offers only circumstantial evidence for the CME mechanism around low-mass stars. Our current data on TIC 234284556 is similarly inconclusive: it is consistent with both the CME and stellar wind scenarios. As demonstrated in Section 6.2, the observed dip depth could theoretically be caused by relatively small mass, so that typical M-dwarf stellar winds remain a plausible explanation. Future data may more tightly constrain the timescales involved in accumulating the asymptotic mass. Observationally, our LCO data already offers us an upper bound on the timescales involved in the postbreakout reappearance of the dip, but the 107 days between the last TESS dip and the LCO dip is too large for us to eliminate either the stellar wind or the CME scenario.

Similarly, as discussed in Section 6.2, the largest eclipse equivalent durations occur in a time period that coincides with the highest flare energy. Given the correlation between flares and coronal mass ejections around the Sun (e.g., Youssef 2012), this could be seen as circumstantial evidence for the CME model, but additional data and further numerical modeling, building on the framework developed by Alvarado-Gómez et al. (2018), would be needed to confirm this hypothesis.

Future observations of TIC 234284556 may offer us a unique way to constrain the mass-accumulation rate and to clarify the relationship between magnetospheric clouds and CMEs. For example, if the reappearance of the dip is shown to be sudden or to occur over timescales too short to be compatible with even the highest estimates of M-dwarf stellar winds, this would suggest a trapped CME as the most likely cause of the dips. Regardless, determining the source of TIC 234284556’s accumulating plasma is an important next step. Considering that direct evidence for extrasolar CMEs is almost nonexistent (Alvarado-Gómez et al. 2020), a trapped CME cause might be especially interesting. However, if stellar winds are the source of the dip, that may allow us to better constrain \dot{M}_{wind} for young and magnetically active low-mass stars.

6.4. In the Context of Young Stars

TIC 234284556, being significantly brighter than many of its analogs, promises to become a benchmark system for understanding a whole class of stars with transiting magnetospheric clouds—systems potentially ranging from the 1.1 Myr B2 star

σ Ori E to the 7–10 Myr binary M dwarf PTFO 8-8695 (Bouma et al. 2020b) to the 5–10 Myr transient flux-dip stars (Stauffer et al. 2017, 2018; Zhan et al. 2019; Stauffer et al. 2021).

This star adds a new name to the short list of flux-dip stars that are candidates for centrifugal breakout, and at only ≈ 44 pc away compared to ≈ 130 pc for the other known centrifugal breakout candidates it is the best choice for follow-up observations. Moreover, at 45 million years old, TIC 234284556 is an older analog to the similar stars in Upper Sco that will allow us to probe a new age range, giving us a better understanding of how centrifugal breakout and magnetospheric clouds work at different evolutionary stages.

We take TIC 234284556 to be a good representative of these other systems, in part because they appear tied together by the following characteristics.

1. *Synchronously rotating dips* not well-explained by a typical transiting planet, but plausibly explained by magnetospheric clouds.
2. *Variable dips* with changing morphology, depth, and duration over relatively short timescales, and typically in a gradual manner.
3. *A lack of an infrared excess*, in contrast with the class of dipper stars.
4. *Asymmetric and triangular dip profiles* in at least some cases.
5. *Youth, and strong rotational signals*, likely due at least in part to the fact that these are correlated with strong magnetic fields.
6. *H α emission*, with the shape consistent across all phases.
7. *One to two dominant dips*, though potentially with smaller secondary ones present. Although this feature could be simple function of geometric orientation rather than probing different physics, we note that this is an observational criterion which distinguishes TIC 234284556 and its closest analogs— σ Ori E, RIK-210, and the other transient flux-dip stars—from more distant relatives like the persistent flux-dip stars, which have been observed to have up to four dips (Stauffer et al. 2017).
8. *Orbital period under 6 days*, a feature common to TIC 234284556, both transient and persistent flux-dip stars, σ Ori E, and PTFO 8-8695.
9. *Occasional sudden disappearances of dips*, sometimes accompanied by an unusually symmetric flare-like event, in a handful of the stars.

More work is needed to clarify which of these characteristics are essential to this emerging class of stars, and to establish where stars that share some, but not all, of these characteristics belong. For example, σ Ori E fits characteristics 1, 3, 5, 6, and 8, but there are two major dips and no noticeable variability in its dips’ characteristics over time (Townsend et al. 2013). Similarly, some of the persistent flux-dip stars have dips that disappear suddenly while accompanied by a flare-like event, but they, like σ Ori E, may have multiple mostly stable dips (Stauffer et al. 2017).

7. Conclusions and Future Work

We have presented our analysis of TIC 234284556, a 45 Myr M dwarf, that has transit-like dips that change in depth and duration over two sectors of TESS data. Besides more gradual depth and duration variations that occur over ~ 10 day timescales, we take note of a sudden disappearance of the dip

over a ~ 1 day period—and then see the dip reappear in LCO data about 100 days later. We have shown that this behavior can be explained by a magnetospheric cloud and centrifugal breakout scenario and have found the data to be inconsistent with other potential explanations. This model broadly matches the numerical predictions of centrifugal breakout for a star with an inclination similar to TIC 234284556 developed by Townsend (2008).

When considered alongside the handful of centrifugal breakout candidates among the known flux-dip stars, we argue that we now have observational evidence that centrifugal breakout plays a role in mass-balancing processes for at least some classes of stars—this despite the fact that previous non-detections of centrifugal breakout led astronomers to consider alternative mass-balancing mechanisms. Moreover, TIC 234284556 hints at the possibility of uniting a class of mysterious young stars ranging from σ Ori E to PTFO 8-8695 and other known flux-dip stars.

However, TIC 234284556 stands out among its potential analogs. It is older, allowing us a glimpse into a different evolutionary stage for this class of stars. It has a long baseline, with more than two years of data, which allows for a better understanding of the transiting dips. This baseline provides the opportunity to observe what appears to be three different dip origins and one phase change, as well as a gradual fading which may be related to recombination of ionized dust during a period of infrequent flares. And, most importantly, TIC 234284556 is the brightest of its class of low-mass stars, making it the best choice for follow-up studies and potentially the archetypal system of this kind.

In particular, future X-ray observations of TIC 234284556 may shed light on the origin and structure of these dips. Simultaneous multi-color time-series photometry, ideally via a southern analog of MuSCAT or MuSCAT2 (Narita et al. 2015, 2019) given TIC 234284556’s decl. δ of -63° , could give a definitive confirmation of the dips’ chromaticity. In-depth comparisons with high-mass stars such as the main-sequence radio pulse emitter CU Vir—a recent centrifugal breakout candidate from Das & Chandra (2021)—may give us insight into how centrifugal magnetospheres vary with spectral type. And tighter photometric constraints on the timescales involved in the reappearance of the dips could allow us to distinguish between the two mass-accumulation mechanisms, CMEs and stellar winds, while potentially adding to currently scanty evidence of extrasolar CMEs or allowing us to more tightly constrain M dwarf stellar wind rates, which, at the moment, are uncertain to five orders of magnitude (Vidotto et al. 2014a).

We thank Richard Townsend, Katja Poppenhaeger, Trevor David, Christina Hedges, and an anonymous referee for thought-provoking conversations and insights into the TIC 234284556 system which improved the quality of this manuscript. We thank Chris Tinney for helpful discussions on Veloce observing modes. E.K.P. thanks Nils Palumbo (University of Wisconsin-Madison) for much-appreciated coding advice, the NEArby Worlds and Their Stars (NEWTS) group (PI: B. Montet, UNSW) for welcoming her into their lab, and the Caltech Beans for moral support throughout the research process.

This paper relies on data from the TESS mission, which is funded by the NASA Explorer Program. TESS data were

obtained from the Mikulski Archive for Space Telescopes (MAST), which is supported in part by the NASA Office of Space Science's grant NNX13AC07G.

This research made use of the SIMBAD database, operated at CDS, Strasbourg, France and of the Exoplanet Follow-up Observation Program (ExoFOP) website, which is operated by the Caltech, under contract with NASA via the Exoplanet Exploration Program.

This work used data from the European Space Agency (ESA) mission Gaia (<https://www.cosmos.esa.int/gaia>), processed by the Gaia Data Processing and Analysis Consortium (DPAC; <https://www.cosmos.esa.int/web/gaia/dpac/consortium>). Funding for the DPAC has been provided by national institutions, in particular the institutions participating in the Gaia Multilateral Agreement.

This work makes use of observations from the Las Cumbres Observatory global telescope network, in particular the Sinistro camera on the LCO-1m telescope at the South African Astronomical Observatory. The LCO observations were conducted under the auspices of NOIRLab program NAO2020B-013 (PI: J. Hartman).

This research also made use of ASAS-SN data. ASAS-SN is funded by the Gordon and Betty Moore Foundation under the 5 year grant GBMF5490 as well as by the National Science Foundation under grants AST-151592 and AST-1908570, with telescopes hosted by LCO.

This work was also based in part on data obtained at the Anglo-Australian Telescope under program A/2020B/09. We acknowledge the traditional owners of the land on which the AAT stands, the Gamilaraay people, and pay our respects to elders past and present.

This material is based upon work supported by the National Science Foundation Graduate Research Fellowship Program under Grant No. DGE-1746045.

E.K.P.'s role in this research was funded by Caltech's Summer Undergraduate Research Fellowship (SURF) program, with generous support from Carl F. Braun and Harold and Mary Zirin.

L.G.B. and J.H. acknowledge support by the TESS GI Program, programs G011103 and G022117, through NASA grants 80NSSC19K0386 and 80NSSC19K1728. J.H. acknowledges additional support from NASA grant NNX17AB61G.

Facilities: TESS, ASAS-SN, LCO (SAAO), Siding Spring Observatory (Veloce), MAST, Simbad.

Software: astropy (Price-Whelan et al. 2018), CurveFit (Caltech 2021) eleanor (Feinstein et al. 2019), emcee (Foreman-Mackey et al. 2013), exoplanet (Foreman-Mackey et al. 2020), itertools (Van Rossum 2020), lightkurve (Lightkurve Collaboration et al. 2018), Mathematica (Wolfram Research 2020), matplotlib (Hunter 2007), numpy (Van Der Walt et al. 2011), os, pickle (Van Rossum 2020), pymc3 (Salvatier et al. 2016), scipy (Virtanen et al. 2020), statsmodels (Seabold & Perktold 2010), stella (Feinstein et al. 2020a), theano (The Theano Development Team et al. 2016), transitleastsquares (Hippeke & Heller 2019), uncertainties (Lebigot 2010).

ORCID iDs

Elsa K. Palumbo  <https://orcid.org/0000-0001-7967-1795>

Benjamin T. Montet  <https://orcid.org/0000-0001-7516-8308>

Adina D. Feinstein  <https://orcid.org/0000-0002-9464-8101>

Luke G. Bouma  <https://orcid.org/0000-0002-0514-5538>

Joel D. Hartman  <https://orcid.org/0000-0001-8732-6166>

Michael A. Gully-Santiago  <https://orcid.org/0000-0002-4020-3457>

Kirsten A. Banks  <https://orcid.org/0000-0001-5210-1696>

References

- Alvarado-Gómez, J. D., Drake, J. J., Cohen, O., Moschou, S. P., & Garraffo, C. 2018, *ApJ*, **862**, 93
- Alvarado-Gómez, J. D., Drake, J. J., Frascchetti, F., et al. 2020, *ApJ*, **895**, 47
- Ansdell, M., Gaidos, E., Rappaport, S. A., et al. 2016, *ApJ*, **816**, 69
- Ansdell, M., Gaidos, E., Hedges, C., et al. 2020, *MNRAS*, **492**, 572
- Aurière, M., Wade, G. A., Silvester, J., et al. 2007, *A&A*, **475**, 1053
- Bailer-Jones, C. A. L., Rybizki, J., Fousneau, M., Demleitner, M., & Andrae, R. 2021, *AJ*, **161**, 147
- Barnes, J. W., van Eyken, J. C., Jackson, B. K., Ciardi, D. R., & Fortney, J. J. 2013, *ApJ*, **774**, 53
- Basri, G., & Nguyen, H. T. 2018, *ApJ*, **863**, 190
- Bell, C. P. M., Mamajek, E. E., & Naylor, T. 2015, *MNRAS*, **454**, 593
- Bell, K. J., Hilton, E. J., Davenport, J. R. A., et al. 2020, *PASP*, **124**, 14
- Belokurov, V., Penoyre, Z., Oh, S., et al. 2020, *MNRAS*, **496**, 1922
- Benz, A. O., & Güdel, M. 2010, *ARA&A*, **48**, 241
- Bodman, E. H. L., Quillen, A. C., Ansdell, M., et al. 2017, *MNRAS*, **470**, 202
- Bohlender, D. A., & Monin, D. 2011, *AJ*, **141**, 169
- Bouma, L. G., Winn, J. N., Ricker, G. R., et al. 2020a, *AJ*, **160**, 86
- Bouma, L. G., Hartman, J. D., Brahm, R., et al. 2020b, *AJ*, **160**, 239
- Boyajian, T. S., LaCourse, D. M., Rappaport, S. A., et al. 2016, *MNRAS*, **457**, 3988
- Briquet, M. 2015, *European Physical Journal Web of Conferences*, **101**, 05001
- Brown, T. M., Baliber, N., Bianco, F. B., et al. 2013, *PASP*, **125**, 1031
- Buemi, C. S., Umama, G., Trigilio, C., & Leto, P. 2007, *A&A*, **462**, 637
- Caltech 2021, http://www.sophphx.caltech.edu/Physics_6/CurveFit/
- Cody, A. M., & Hillenbrand, L. A. 2010, *ApJS*, **191**, 389
- Cody, A. M., & Hillenbrand, L. A. 2018, *AJ*, **156**, 71
- Cranmer, S. R. 2017, *ApJ*, **840**, 114
- Crundall, T. D., Ireland, M. J., Krumholz, M. R., et al. 2019, *MNRAS*, **489**, 3625
- Cutri, R. M., Skrutskie, M. F., van Dyk, S., et al. 2003, 2MASS All Sky Catalog of Point Sources (Washington, DC: NASA)
- Cutri, R. M., Wright, E. L., Conrow, T., et al. 2021, *yCat*, II/328
- Das, B., & Chandra, P. 2021, *ApJ*, **921**, 9
- Davenport, J. R. A., Mendoza, G. T., & Hawley, S. L. 2020, *AJ*, **160**, 36
- David, T. J., Petigura, E. A., Hillenbrand, L. A., et al. 2017, *ApJ*, **835**, 168
- DENIS Consortium 2005, *yCat*, **2263**
- Donati, J. F., & Landstreet, J. D. 2009, *ARA&A*, **47**, 333
- Faigler, S., Tal-Or, L., Mazeh, T., Latham, D. W., & Buchhave, L. A. 2013, *ApJ*, **771**, 26
- Feigelson, E. D., Giampapa, M. S., & Vrba, F. J. 1991, in *The Sun in Time*, ed. C. P. Sonett, M. S. Giampapa, & M. S. Matthews (Tucson, AZ: Univ. Arizona Press)
- Feinstein, A., Montet, B., & Ansdell, M. 2020a, *JOSS*, **5**, 2347
- Feinstein, A. D., Montet, B. T., Ansdell, M., et al. 2020b, *AJ*, **160**, 219
- Feinstein, A. D., Montet, B. T., Foreman-Mackey, D., et al. 2019, *PASP*, **131**, 094502
- Foreman-Mackey, D., Agol, E., Ambikasaran, S., & Angus, R. 2017, *AJ*, **154**, 220
- Foreman-Mackey, D., Hogg, D. W., Lang, D., & Goodman, J. 2013, *PASP*, **125**, 306
- Foreman-Mackey, D., Luger, R., Czekala, I., et al. 2020, *exoplanet-dev/exoplanet v0.3.2*, doi:10.5281/zenodo.1998447
- Gagné, J., Mamajek, E. E., Malo, L., et al. 2018, *ApJ*, **856**, 23
- Gaia Collaboration 2020, *yCat*, I/350
- Gaia Collaboration, Brown, A. G. A., Vallenari, A., et al. 2021, *A&A*, **649**, A1
- Getman, K. V., & Feigelson, E. D. 2021, *ApJ*, **916**, 32
- Gilbert, J., Bergmann, C., Bloxham, G., et al. 2018, *Proc. SPIE*, **10702**, 107020Y
- Gregory, S. G., Donati, J. F., Morin, J., et al. 2012, *ApJ*, **755**, 97
- Groote, D., & Hunger, K. 1977, *A&A*, **56**, 129
- Grunhut, J. H., Wade, G. A., Leutenegger, M., et al. 2013, *MNRAS*, **428**, 1686
- Günther, M. N., Berardo, D. A., Ducrot, E., et al. 2020a, *arXiv:2008.11681*
- Günther, M. N., Zhan, Z., Seager, S., et al. 2020b, *AJ*, **159**, 60

- Hamann, A., Montet, B. T., Fabrycky, D. C., Agol, E., & Kruse, E. 2019, *AJ*, **158**, 133
- Hauschildt, P. H., Allard, F., & Baron, E. 1999, *ApJ*, **512**, 377
- Hedges, C., Hodgkin, S., & Kennedy, G. 2018, *MNRAS*, **476**, 2968
- Herrero, E., Lanza, A. F., Ribas, I., et al. 2014, *A&A*, **563**, A104
- Hippke, M., & Heller, R. 2019, *A&A*, **623**, A39
- Honda, S., Notsu, Y., Namekata, K., et al. 2018, *PASJ*, **70**, 62
- Howard, W. S., Corbett, H., Law, N. M., et al. 2020, *ApJ*, **902**, 115
- Hubrig, S., & Schöller, M. 2019, *Astronomical Polarisation from the Infrared to Gamma Rays*, Vol. 173 (Basel: Springer)
- Hunt-Walker, N. M., Hilton, E. J., Kowalski, A. F., Hawley, S. L., & Matthews, J. M. 2012, *PASP*, **124**, 545
- Hunter, J. D. 2007, *CSE*, **9**, 90
- Jardine, M., & Collier Cameron, A. 2019, *MNRAS*, **482**, 2853
- Jardine, M., Collier Cameron, A., Donati, J. F., & Hussain, G. A. J. 2020, *MNRAS*, **491**, 4076
- Jayasinghe, T., Kochanek, C. S., Stanek, K. Z., et al. 2021, *MNRAS*, **503**, 200
- Jenkins, J. M., Twicken, J. D., McCauliff, S., et al. 2016, *Proc. SPIE*, **9913**, 99133E
- Kobayashi, H., Kimura, H., Watanabe, S. I., Yamamoto, T., & Müller, S. 2011, *EP&S*, **63**, 1067
- Kochukhov, O. 2021, *A&ARv*, **29**, 1
- Kowalski, A. F., Hawley, S. L., Wisniewski, J. P., et al. 2013, *ApJS*, **207**, 15
- Kraus, A. L., Shkolnik, E. L., Allers, K. N., & Liu, M. C. 2014, *AJ*, **147**, 146
- Kretzschmar, M. 2011, *A&A*, **530**, A84
- Landstreet, J. D., & Borra, E. F. 1978, *ApJL*, **224**, L5
- Lebigot, E. 2010, <https://uncertainties-python-package.readthedocs.io/en/latest/>
- Lieshout, R. V., & Rappaport, S. A. 2018, in *Handbook of Exoplanets*, ed. H. J. Deeg & J. A. Belmonte (Berlin: Springer)
- Lightkurve Collaboration, Cardoso, J. V. D. M., Hedges, C., et al. 2018, *Lightkurve: Kepler and TESS time series analysis in Python*, *Astrophysics Source Code Library*, ascl:1812.013
- Loeb, A., & Gaudi, B. S. 2003, *ApJL*, **588**, L117
- Maehara, H., Notsu, Y., Namekata, K., et al. 2021, *PASJ*, **73**, 44
- Mandel, K., & Agol, E. 2002, *ApJL*, **580**, L171
- Mann, A. W., Johnson, M. C., Vanderburg, A., et al. 2020, *AJ*, **160**, 179
- Mazeh, T., & Faigler, S. 2010, *A&A*, **521**, L59
- McGinnis, P. T., Alencar, S. H. P., Guimarães, M. M., et al. 2015, *A&A*, **577**, A11
- McLaughlin, D. B. 1924, *ApJ*, **60**, 22
- Montet, B. T., Feinstein, A. D., Luger, R., et al. 2020, *AJ*, **159**, 112
- Morin, J., Donati, J. F., Petit, P., et al. 2010, *MNRAS*, **407**, 2269
- Narita, N., Fukui, A., Kusakabe, N., et al. 2015, *JATIS*, **1**, 045001
- Narita, N., Fukui, A., Kusakabe, N., et al. 2019, *JATIS*, **5**, 015001
- Newton, E. R., Irwin, J., Charbonneau, D., et al. 2017, *ApJ*, **834**, 85
- Oksala, M. E., Wade, G. A., & Townsend, R. H. D. 2012, *MNRAS*, **419**, 959
- Oksala, M. E., Kochukhov, O., Krůčka, J., et al. 2015, *MNRAS*, **451**, 2015
- Onitsuka, M., Fukui, A., Narita, N., et al. 2017, *PASJ*, **69**, L2
- Osten, R., Livio, M., Lubow, S., et al. 2013, *ApJL*, **765**, L44
- Osten, R. A., & Wolk, S. J. 2015, *ApJ*, **809**, 79
- Owoccki, S. P., & Cranmer, S. R. 2018, *MNRAS*, **474**, 3090
- Owoccki, S. P., Shultz, M. E., ud-Doula, A., et al. 2020, *MNRAS*, **499**, 5366
- Pál, A. 2012, *MNRAS*, **421**, 1825
- Price-Whelan, A. M., Sipőcz, B. M., Günther, H. M., et al. 2018, *AJ*, **156**, 123
- Rappaport, S., Levine, A., Chiang, E., et al. 2012, *ApJ*, **752**, 1
- Reiners, A., Joshi, N., & Goldman, B. 2012, *AJ*, **143**, 93
- Reinhold, T., & Gizon, L. 2015, *A&A*, **583**, A65
- Ricker, G. R., Winn, J. N., Vanderspek, R., et al. 2014, *Proc. SPIE*, **9143**, 914320
- Rivinius, T., Townsend, R. H. D., Kochukhov, O., et al. 2013, *MNRAS*, **429**, 177
- Rizzuto, A. C., Newton, E. R., Mann, A. W., et al. 2020, *AJ*, **160**, 33
- Rossiter, R. A. 1924, *ApJ*, **60**, 15
- Salvatier, J., Wiecki, T. V., & Fonnesbeck, C. 2016, *PeerJ Computer Science*, **2**, e55
- Sanchis-Ojeda, R., Rappaport, S., Pallè, E., et al. 2015, *ApJ*, **812**, 112
- Scholz, A., Coffey, J., Brandeker, A., & Jayawardhana, R. 2007, *ApJ*, **662**, 1254
- Seabold, S., & Perktold, J. 2010, in *9th Python in Science Conf.*, ed. E. Jones & J. Millman (Austin, TX: SciPy), 92
- Shappee, B. J., Prieto, J. L., Grupe, D., et al. 2014, *ApJ*, **788**, 48
- Shultz, M. E., Owoccki, S., Rivinius, T., et al. 2020, *MNRAS*, **499**, 5379
- Shulyak, D., Reiners, A., Nagel, E., et al. 2019, *A&A*, **626**, A86
- Stassun, K. G., Oelkers, R. J., Pepper, J., et al. 2018, *AJ*, **156**, 102
- Stassun, K. G., Oelkers, R. J., Paegert, M., et al. 2019, *AJ*, **158**, 138
- Stauffer, J., Cody, A. M., McGinnis, P., et al. 2015, *AJ*, **149**, 130
- Stauffer, J., Collier Cameron, A., Jardine, M., et al. 2017, *AJ*, **153**, 152
- Stauffer, J., Rebull, L., David, T. J., et al. 2018, *AJ*, **155**, 63
- Stauffer, J., Rebull, L. M., Jardine, M., et al. 2021, *AJ*, **161**, 60
- Tanimoto, Y., Yamashita, T., Ui, T., et al. 2020, *PASJ*, **72**, 23
- Theano Development Team, AI-Rfou, R., Alain, G., et al. 2016, [arXiv:1605.02688](https://arxiv.org/abs/1605.02688)
- Tielens, A. G. G. M. 2005, *The Physics and Chemistry of the Interstellar Medium* (Cambridge: Cambridge Univ. Press)
- Townsend, R. H. D. 2007, in *ASP Conf. Ser. 361, Active OB-Stars: Laboratories for Stellar and Circumstellar Physics*, ed. A. T. Okazaki, S. P. Owoccki, & S. Steff (San Francisco, CA: ASP), 110
- Townsend, R. H. D. 2008, *MNRAS*, **389**, 559
- Townsend, R. H. D., & Owoccki, S. P. 2005, *MNRAS*, **357**, 251
- Townsend, R. H. D., Rivinius, T., Rowe, J. F., et al. 2013, *ApJ*, **769**, 33
- Ud-Doula, A., Owoccki, S. P., & Townsend, R. H. D. 2008, *MNRAS*, **385**, 97
- ud-Doula, A., Townsend, R. H. D., & Owoccki, S. P. 2006, *ApJL*, **640**, L191
- Van Der Walt, S., Colbert, S. C., & Varoquaux, G. 2011, *CSE*, **13**, 22
- van Eyken, J. C., Ciardi, D. R., von Braun, K., et al. 2012, *ApJ*, **755**, 42
- Van Rossum, G. 2020, *The Python Library Reference*, release 3.8.2 (Python Software Foundation)
- Vanderburg, A., Johnson, J. A., Rappaport, S., et al. 2015, *Natur*, **526**, 546
- Vidotto, A. A., Jardine, M., Morin, J., et al. 2014a, *MNRAS*, **438**, 1162
- Vidotto, A. A., Gregory, S. G., Jardine, M., et al. 2014b, *MNRAS*, **441**, 2361
- Virtanen, P., Gommers, R., Oliphant, T. E., et al. 2020, *NatMe*, **17**, 261
- Waggoner, A. R., & Cleeves, L. I. 2019, *ApJ*, **883**, 197
- Waugh, R. F. P., Jardine, M. M., Morin, J., & Donati, J. F. 2021, *MNRAS*, **505**, 5104
- Williams, J. P., & Cieza, L. A. 2011, *ARA&A*, **49**, 67
- Wolfram Research 2020, *Mathematica*, v. 12.2, <https://www.wolfram.com/mathematica>
- Youssef, M. 2012, *JAsGe*, **1**, 172
- Yu, L., Winn, J. N., Gillon, M., et al. 2015, *ApJ*, **812**, 48
- Zacharias, N., Finch, C. T., Girard, T. M., et al. 2012, *yCat*, **1/322A**
- Zaire, B., Donati, J.-F., & Klein, B. 2021, *MNRAS*, **504**, 1969
- Zhan, Z., Günther, M. N., Rappaport, S., et al. 2019, *ApJ*, **876**, 127